Annual Review of Fluid Mechanics

Elastic Turbulence: An Experimental View on Inertialess Random Flow

Victor Steinberg[1,2]

[1]Department of Physics of Complex Systems, Weizmann Institute of Science, Rehovot 76100, Israel; email: victor.steinberg@weizmann.ac.il

[2]The Racah Institute of Physics, Hebrew University of Jerusalem, Jerusalem 91904, Israel

Annu. Rev. Fluid Mech. 2021. 53:27–58

The *Annual Review of Fluid Mechanics* is online at fluid.annualreviews.org

https://doi.org/10.1146/annurev-fluid-010719-060129

Keywords

elastic instabilities, elastic turbulence, coil–stretch transition, elastic waves, wall-dominated elastic turbulence, inertial effect in elastic turbulence

Abstract

A viscous solvent laminar flow may be strongly modified by the addition of a tiny amount of long polymer molecules, resulting in a chaotic flow called elastic turbulence (ET). ET is attributed to polymer stretching, which generates elastic stress and its back reaction on the flow. Its properties are analogous to those observed in hydrodynamic turbulence, although the formal similarity does not imply a similarity in physical mechanisms underlining these two types of random motion. Here we review the statistical and spectral properties and the spatial structure of the velocity field, the statistical and spectral properties of pressure fluctuations, and scaling of the friction factor of ET in wall-bounded and unbounded flow geometries, as observed in experiments and numerical simulations and described by theory for a wide range of control parameters and polymer concentrations.

1. INTRODUCTION

A small addition of long-chain flexible polymer molecules strongly affects both laminar and turbulent flows of Newtonian solvents due to polymer stretching, which generates elastic stress, causing the polymer solution to be elastic and providing a memory to the fluid flow. As a result, many properties of a polymer solution flow (especially a dilute one) can be understood from the dynamics of a single polymer, which experiences the combined action of stretching by the flow and elastic relaxation. In laminar flows, elastic instabilities (Larson 1992, Shaqfeh 1996, Groisman & Steinberg 1998a) and elastic turbulence (ET) (Groisman & Steinberg 2000, 2001b) are observed at Reynolds number $Re < 1$ and Weissenberg number $Wi \gg 1$, whereas in turbulent flows, turbulent drag reduction (TDR) occurs at $Re \gg 1$ and $Wi \gg 1$ (Toms 1949). Here the control parameters $Re = \rho UL/\eta$ and $Wi = \lambda U/L$ are defined via the mean fluid speed U, the vessel size L, the fluid density ρ, the dynamic viscosity η, and the longest polymer relaxation time λ. However, the critical difference between these two control parameters is that Re is defined by a velocity, whereas Wi is defined via a velocity gradient, or shear rate. This review presents a predominantly experimental point of view on ET, a chaotic flow without inertia driven solely by the nonlinear elastic stress generated by polymers stretched by the flow above the elastic instability. Both macro- and microscopic approaches to investigate ET are addressed, as well as the role of inertial effects in altering ET properties. The last of these topics is necessary to establish the missing links among ET, elasto-inertial turbulence (EIT) (Samanta et al. 2013), and TDR (Toms 1949).

Despite the fact that ET was discovered just two decades ago, its potential use has emerged in various industrial applications, such as the effective mixing of viscous fluids particularly in microfluidic curvilinear channels at $Re \ll 1$ (Groisman & Steinberg 2001b, Burghelea et al. 2004a, Gan et al. 2006) and, relatedly, the enhancement of heat transport in microchannels, investigated in detail by Traore et al. (2015), Whalley et al. (2015), Abed et al. (2016), and Li et al. (2017). Furthermore, efficient oil droplet emulsification and destroying capillary effects have been observed (Slutsky & Steinberg 2005, Poole et al. 2012), but most of all a significant intensification of crude oil recovery compared to traditional chemical flooding has been established (Clarke et al. 2015, Howe et al. 2015, Mitchell et al. 2016).

Similar to hydrodynamic turbulence, the properties of ET are significantly altered by the presence of walls. For this reason, we first discuss the ET properties relevant to a homogeneous and isotropic velocity field used in theoretical models of ET. Then, we present the properties of wall-dominated ET, in which a boundary layer modifies velocity flow structures, spectral properties, and the statistics of the velocity field.

2. PURE ELASTIC INSTABILITIES AS PRECURSORS OF ELASTIC TURBULENCE IN CURVILINEAR FLOWS

The elastic stress engendered by polymer stretching is the only source of nonlinearity for polymer solution flow at $Re \ll 1$ coming from a constitutive equation for elastic stress σ (Bird et al. 1987). As a result, an elastic instability of a laminar flow results when the elastic energy overcomes the dissipation due to polymer relaxation, the ratio of which defines the main control parameter, the Weissenberg number, $Wi \sim \lambda(U\nabla)\sigma/\sigma \sim \lambda U/L = \lambda/\tau_u$, where $\tau_u = L/U$ is the hydrodynamic timescale. In shear flow, the elastic stress is anisotropic and characterized by the first normal stress difference, $N_1 = \sigma_{11}–\sigma_{22}$, where σ_{11} and σ_{22} are the diagonal components of the stress tensor along the flow velocity and the velocity gradient directions, respectively. In curvilinear shear flow, which we consider in this review only in the context of elastic instabilities and ET, N_1 gives a rise to a volume force termed the hoop stress acting on the fluid in the direction of the curvature. The hoop stress is a driving force for the rod-climbing effect (Bird et al. 1987) as well as for elastic

instability. Pure elastic instabilities at $Re \ll 1$ are observed in a large variety of curvilinear flow geometries, from Couette flow between two cylinders, where an intrinsic instability mechanism has been suggested (Larson et al. 1990) and quantitatively verified experimentally (Groisman & Steinberg 1998a,b; Steinberg & Groisman 1998), to swirling flows between two rotating parallel disks (McKinley et al. 1991, Oeztekin & Brown 1993, Byars et al. 1994), cone-and-plate geometries (Oeztekin et al. 1994), curvilinear channels or Dean flow (Joo & Shaqfeh 1992; Burghelea et al. 2004a,b; Groisman & Steinberg 2004; Jun & Steinberg 2011; Soulies et al. 2017), cross-channel flow (Arratia et al. 2006, Poole et al. 2007, Haward & McKinley 2013, Varshney et al. 2016), and wake instability in flows past a single obstacle, past an array of obstacles, or between two obstacles (McKinley et al. 1993, Khomami & Moreno 1997, Vázquez-Quesada & Ellero 2012, Grilli et al. 2013, Kenney et al. 2013, Varshney & Steinberg 2017). Early results on elastic instabilities have been reviewed by Larson (1992) and Shaqfeh (1996).

2.1. Taylor–Couette Instabilities

The common ingredient in mechanisms of Taylor–Couette (TC) instabilities is the hoop stress as a driving factor. Elastic instabilities and their succession are best documented and analyzed both theoretically and experimentally in TC flow between two coaxial cylinders, a paradigm of bifurcations and pattern selection in Newtonian and viscoelastic fluids (Drazin & Reid 1982, Cross & Hohenberg 1993).

The addition of long polymers at low concentrations qualitatively alters the bifurcation sequence in TC flow and the bifurcation onset due to elastic stress generated by polymers stretched by basic Couette flow. The ratio of the inertial to elastic stresses is defined by the elasticity, $El = Wi/Re = \lambda/\tau_{visc} = \lambda\eta_s/\rho L^2$, where $\tau_{visc} = L^2\rho/\eta_s$ is the viscous diffusion time. Thus, the stability of TC flow (as well as other flow geometries) in a polymer solution is defined by three control parameters, Re, El, and ϕ/ϕ^* [or η_p/η_s, given $\eta_p = f(\phi/\phi^*)$], where ϕ and ϕ^* are the polymer concentration and polymer overlapped concentration, respectively, and η_s and η_p are the solvent viscosity and the polymer contribution to the solution viscosity, respectively (Bird et al. 1987). Thus, the three-dimensional (3D) parameter space may include a codimension-two line, where two modes simultaneously become unstable and the pattern dynamics is more evolved (Brand et al. 1984, Groisman & Steinberg 1996). For constant ϕ, by varying η_s and ρ, one can scan a 2D stability diagram in (Re, El) coordinates from inertia-dominated flows at $El \ll 1$ to elasticity-dominated flows at $El \gg 1$ (Groisman & Steinberg 1996, 1998b; Steinberg & Groisman 1998). Early studies of inertio-elastic instabilities in TC flow of a viscoelastic fluid, reviewed by Larson (1992), concentrated on the slight variations of the first instability at $El < 1$ by changing ϕ. However, due to a poor rheological characterization of fluids, only a qualitative comparison of theory and experimental results was possible. Larson et al. (1990) published a pioneering result on the purely elastic instability in TC flow of a non-shear-thinning (Boger) fluid, presenting both experimental evidence of the elastic instability and the first linear stability analysis. The main experimental breakthrough of this study was the use of a dilute polymer solution with a highly viscous solvent, which provided a constant solution viscosity at $El \gg 1$ and allowed for a complete characterization of the solution's rheological properties, which fit well the properties of the Oldroyd-B model used in the theory, allowing for a quantitative comparison with the experimental results. The main proof of the pure elastic nature of the transition was its appearance at the rotation of either inner or outer cylinders, which excluded inertial effects (Larson et al. 1990). The main theoretical breakthrough was an explanation of the instability mechanism for axisymmetric perturbations and the resulting stability criterion. The instability mechanism is based on a coupling of the radial velocity gradient perturbations to the basic azimuthal shear, enhancing a radial bulk force, which takes energy from

the primary azimuthal flow to reinforce the radial flow. Due to the time delay between polymer stretching and the radial force enhancement caused by polymer relaxation, the instability appears to be time dependent.

2.2. Differences Between Experiment and Theory

However, experimental observations of the TC pure elastic instability by Muller et al. (1989, 1993), Larson et al. (1990, 1994), Larson (1992), and Baumert & Muller (1995, 1997, 1999) have revealed qualitative and quantitative discrepancies with Larson et al.'s (1990) theoretical predictions. First, the experiments revealed extremely long timescales to develop a secondary flow compared to those of the velocity field and λ. Second, experimental observations of patterns above the instability onset by Muller et al. (1989, 1993), Larson et al. (1990, 1994), Larson (1992), and Baumert & Muller (1995, 1997, 1999) are contradictory and report an oscillatory instability and stationary axisymmetric vortices. Finally, the experimental value of the instability onset, Wi_c, was found to be up to an order of magnitude lower than what the theory predicted (Baumert & Muller 1995, 1997). These discrepancies cast doubt on the relevance of the experiments to Larson et al.'s (1990) theory. The puzzle has been resolved by suggesting that the experiments were conducted at nonisothermal conditions due to viscous dissipation heating, in contrast to the theory developed for isothermal ones (Al-Mubaiyedh et al. 1999). Thus, it has been demonstrated (Al-Mubaiyedh et al. 2000, 2002) that a long timescale is associated with the development of a steady-state temperature profile and that the most unstable mode is stationary and axisymmetric, with Wi_c an order of magnitude lower than the value obtained by Larson et al. (1990). Al-Mubaiyedh et al.'s (1999, 2000, 2002) theory based on the nonisothermal conditions agrees with earlier experiments (Muller et al. 1989, 1993; Larson et al. 1990, 1994; Larson 1992; Baumert & Muller 1995, 1997, 1999), as well as later ones (White & Muller 2000, 2003), and the main conclusion of this agreement is that the experimental results mentioned above were obtained in nonisothermal conditions and cannot be compared with either Larson et al.'s (1990) theory or subsequent experiments performed in isothermal conditions.

2.3. Bifurcations

Further theoretical analysis of TC flow of a viscoelastic fluid (Avgousti & Beris 1993, Joo & Shaqfeh 1994, Sureshkumar et al. 1994) has clarified that the most unstable modes, axially driven spirals and rotating standing waves (RSWs), or ribbons, are nonaxisymmetric and time dependent, with at least one of them being subcritical (Sureshkumar et al. 1994), in contrast to Larson et al.'s (1990) early finding and in quantitative agreement with experiments by Groisman & Steinberg (1996, 1997, 1998a,b) and Steinberg & Groisman (1998). A striking influence of El on pattern selection above the first bifurcation is observed even at $El \ll 1$ (Groisman & Steinberg 1996, 1998b; Steinberg & Groisman 1998), whereas at $El \gg 1$, solely elastically driven instabilities and patterns are found at $Wi > Wi_c$ (Groisman & Steinberg 1996, 1997, 1998a,b; Steinberg & Groisman 1998). The elasticity El varies by three orders of magnitude by changing η_s with fixed ϕ/ϕ^* and separately by changing ϕ/ϕ^* in a wide range of 10–300 ppm at the fixed El, where ϕ^* is approximately 1,000 ppm for polyacrylamide (PAM) with a molecular weight of $M_w = (5–6) \times 10^6$ Da. The regions of weak and strong El are separated by the codimension-two point at El_{ct}, and the sequence of instabilities and selected patterns at $El < El_{ct}$ varies depending on ϕ/ϕ^*. The value of El_{ct} grows with ϕ for fixed η_s, as $El_{ct} = 0.0041 + 0.093\phi/\phi^*$ for $0.01 < \phi/\phi^* < 0.3$, as found from the fit (Groisman 1993). At $El < El_{ct}$, one observes two elastically modified oscillatory, nonaxisymmetric RSWs, or ribbons, and disordered oscillations (DOs), while at $El > El_{ct}$, for all ϕ/ϕ^*, one finds DOs, nonaxisymmetric and axisymmetric oscillatory strips (OSs), and solitary vortex pair patterns

termed diwhirls (DWs). Closer to El_{ct}, only DOs are observed above the backward elastic instability, which becomes increasingly hysteretic with growing El (Groisman & Steinberg 1996, 1998b). Moreover, at $El > El_{ct}$, unstable nonaxisymmetric standing waves, similar to steady RSWs, are detected in a transient flow toward DOs. The quantitative verification of the purely elastic instability criterion is obtained at $El \gg El_{ct}$ when DOs appear at $Wi_c \approx 25$, independent of El; Re becomes irrelevant; and the predicted strongly hysteretic bifurcation (Sureshkumar et al. 1994) of the nonaxisymmetric mode (Joo & Shaqfeh 1994, Sureshkumar et al. 1994) is confirmed. By decreasing Wi from Wi_c back into the hysteretic region, one finds the sequence of nonaxisymmetric and axisymmetric OSs and DWs, all with strong asymmetry between inflow and outflow (Groisman & Steinberg 1997, 1998a,b; Steinberg & Groisman 1998). The breaking inflow/outflow symmetry is a direct consequence of the coupling between the radial velocity gradient perturbations and the hoop stress, an inherent feature of the instability mechanism (Larson et al. 1990). Besides RSWs, the later experiments with water solutions of polyethyleneoxde with a molecular weight of $M_w = 8 \times 10^6$ Da at $10^{-3} < El < 0.4$ and $0 \leq \phi \leq 700$ ppm have revealed an elastically modified wavy vortex pattern (Crumeyrolle et al. 2002). However, due to the variations in both λ and η by changing only ϕ and due to the different definition of El in terms of η instead of η_s, the resulting experimental path hinders a comparison with the experiments and theory presented above. Further, it has been shown that a transition from RSWs to DOs at $El < El_{ct}$ occurs via a nucleation of spatiotemporal defects in RSWs (Latrache et al. 2016).

From the theoretical side, the localized nonlinear flow pattern, DWs, is confirmed to be the fundamental building block of the spatiotemporal dynamics of elastic fluid flow, with its structure and self-sustained mechanism similar to that identified by experiment (Kumar & Graham 2000). Later 3D numerical studies of spatiotemporal pattern dynamics in a wide range of El and Re have shown good agreement with experiment in velocity spectral properties, drag forces, molecular conformations, and viscoelastic stresses (Thomas et al. 2006, 2009).

3. ELASTIC TURBULENCE AND ITS MAIN PROPERTIES: MACROSCOPIC AND MICROSCOPIC APPROACHES

3.1. Discovery of Elastic Turbulence and Its Main Properties: Macroscopic Approach

The earliest observations of ET in the 1960s and 1970s referred mostly either to visual observations of surface irregularities of polymer melts and extremely viscous entangled polymer solutions, which were associated with an abrupt rise in the flow rate, contrary to what is expected for turbulence (Vinogradov & Ivanova 1967), or to ET connected with irregularities in the discharged jet of a dilute polymer solution (Giesekus 1968), but these discussions did not make any attempt to characterize or compare the flow with high-Re turbulence (e.g., Giesekus 1972). Moreover, in detailed reviews (Larson 1992, Shaqfeh 1996), these results on ET were either ignored or the proposed explanations were referred to as wall slip and constitutive instabilities (see also Denn 1990).

Groisman & Steinberg (2000, 2001b) first reported the discovery of the main features of ET and in a quantitative characterization suggested the analogy of a highly irregular flow of a dilute polymer solution in a swirling flow between rotating and stationary disks, as well as in a serpentine channel flow, both with curvilinear streamlines at $Re < 1$ and inertial turbulence at $Re \gg 1$. There are three main features by which ET is identified in both flow geometries (Groisman & Steinberg 2000, 2001b) and high-Re turbulence (Landau & Lifschitz 1987, Tritton 1988): (*a*) a large increase in the flow resistance compared to laminar flow at the same Re, (*b*) a broad range of spatiotemporal scales with a steep power law decay in velocity power spectra, and (*c*) an orders-of-magnitude

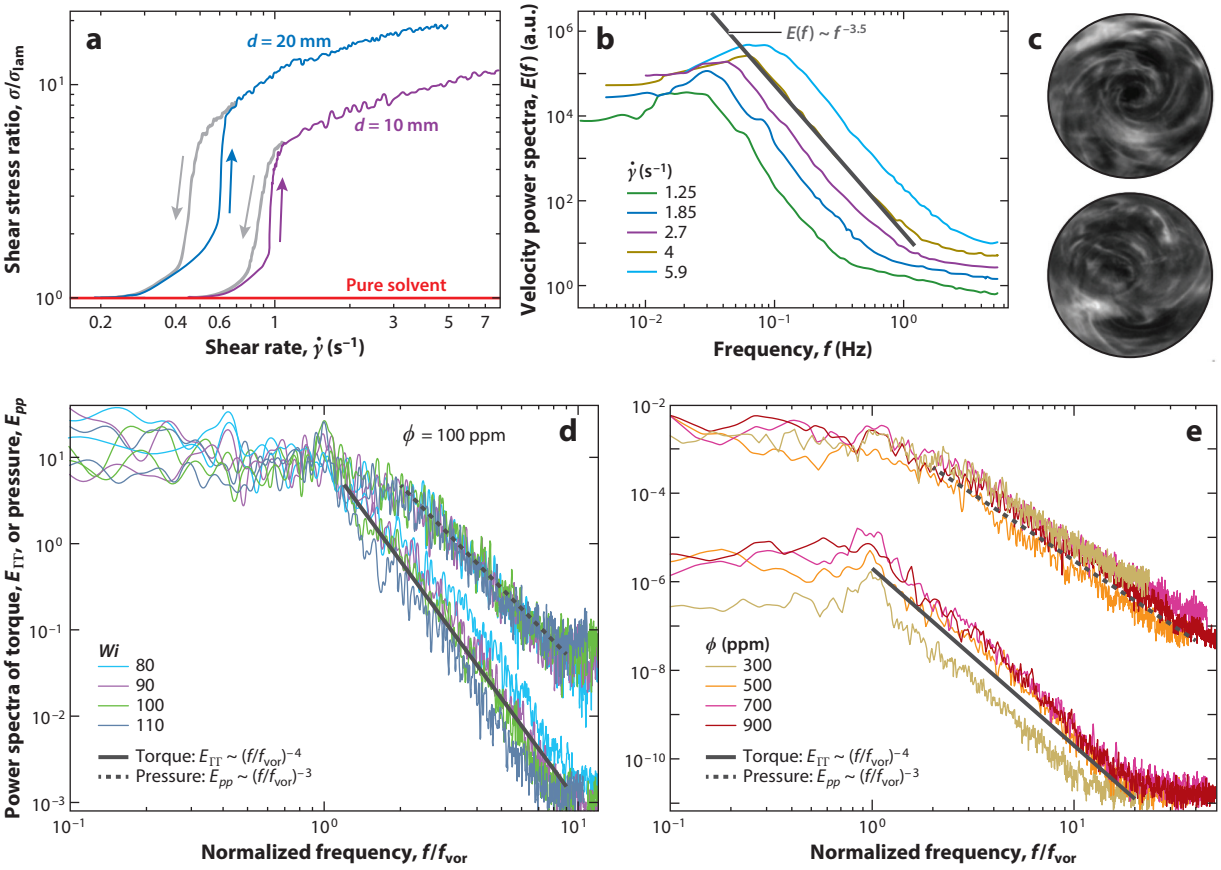

Figure 1

(*a*) The average shear stress ratio $\sigma/\sigma_{\text{lam}}$, or the flow resistance, versus the shear rate $\dot{\gamma}$, for two gap values between two disks, $d = 10$ mm and 20 mm, and a pure solvent. The experimental setup (not shown; Groisman & Steinberg 2000) consists of a stationary cylindrical cup with a plain bottom (the lower stationary disk; radius 43.6 mm), concentric with a rotating upper disk (radius 38 mm) attached to the shaft of a commercial rheometer, which just touches the surface of a solution of 65% saccharose and 1% NaCl in water with viscosity 0.324 Pa·s as a solvent for the polymer, to which has been added polyacrylamide of molecular weight $M_w = 18{,}000{,}000$ Da at a concentration of 80 ppm by weight. The walls of the cup are transparent to allow laser Doppler velocimetry measurements. The lower disk is also transparent and, together with a mirror tilted by 45° placed under the lower disk, provides viewing access from below using a CCD (charge-coupled device) camera mounted at the side. The temperature in the setup is stabilized by circulating air in a closed box and by circulating water at 12°C under a steel lower plate. (*b*) Frequency power spectra $E(f)$ of velocity fluctuations at the center of the swirling flow with approximately zero average velocity for five values of $\dot{\gamma}$ above the transition value of $\dot{\gamma}_{\text{tr}} \approx 1\ \text{s}^{-1}$. A fit at $\dot{\gamma} = 4\ \text{s}^{-1}$ over a decade in f gives $E(f) \sim f^{-3.5}$. (*c*) Two snapshots of irregular flow structures at $Wi = 13$ and $Re = 0.7$, visualized by suspended, light-reflecting flakes. (*d*) Power spectra of torque $E_{\Gamma\Gamma}$ and pressure E_{pp} fluctuations as functions of the normalized frequency, f/f_{vor}, for a polymer concentration of $\phi = 100$ ppm and various values of Wi. (*e*) $E_{\Gamma\Gamma}$ and E_{pp} as functions of f/f_{vor} for different ϕ at maximum Wi. The value of the main vortex frequency, f_{vor}, is obtained from the peaks in the Γ and p power spectra versus Wi. Panels adapted with permission from (*a–c*) Groisman & Steinberg (2000), and (*d*,*e*) Jun & Steinberg (2017).

increase in mixing rate compared with diffusion (see **Figure 1*a–c***) (Groisman & Steinberg 2000, 2001b). This formal similarity in the main features is the reason for calling this low-*Re* chaotic flow "elastic turbulence."

However, the similarities between the two random flows do not imply the same underlying physical mechanism. Contrary to inertial turbulence driven by Reynolds stress with a local

transfer of energy flux in the inertial-scale range, ET is driven solely by the elastic stress without inertia, and the algebraic velocity power spectrum decay is not related to the energy cascade and any conservation law, since the main energy dissipation occurs at all scales. Here the leading mechanism of small-scale generation occurs via stretching and folding of the elastic stress field during random advection of a fluid element by the fluctuating velocity field at the largest scales. A back reaction of the elastic stress field on the flow (dynamo effect) leads to a stationary dynamical state of ET. The dynamics of elastic stress in ET is analogous to magnetic stress in a small-scale fast dynamo in magneto-hydrodynamics (MHD) (see Tritton 1988, Landau & Lifschitz 1989) and to turbulent advection of a passive scalar in the Batchelor regime below the dissipation scale ζ of high-Re turbulence (Batchelor 1959). In contrast to the latter two systems, there is currently no technique to directly measure elastic stress in ET that strongly limits its complete experimental characterization. Currently the only ways to evaluate the elastic stress are either from spatial and temporal velocity gradient fields or, as discussed below, from polymer stretching as well as elastic wave speed.

Thus, the key experimental observation in ET is the power law decay of the velocity power spectra in a frequency domain, $E(f) \sim f^{-\alpha}$, with the exponent $\alpha > 3$ between 3.3 and 3.6 depending on the flow geometry (Groisman & Steinberg 2000, 2001b). Since the validity of the Taylor hypothesis is also justified with some limitations in ET shear flow (Burghelea et al. 2005), one expects the same exponent value in both the f and k domains, although $\alpha = 3.5$ in the k domain is also obtained by particle image velocimetry (PIV) only in a shorter-scale range (Burghelea et al. 2007). Due to the steep decay of the velocity spectrum leading to a sharp reduction in the contribution of higher-order modes, the velocity and velocity gradient fields are both determined by large spatial scales on the order of the vessel size, which is the main evidence of the velocity field smoothness. Thus, ET is essentially a spatially smooth and temporally random flow, dominated by a strong nonlinear interaction of a few large-scale spatial modes. This type of random flow appears in inertial turbulence below ζ (Batchelor 1959).

As discovered later (Jun & Steinberg 2009, 2017), frequency power spectra of both torque, Γ, and pressure, p, fluctuations have a high signal-to-noise ratio in the ET regime of a swirling flow. As a result, one observes algebraic decays of the torque, $E_{\Gamma\Gamma}$, and pressure, E_{pp}, power spectra fluctuations, another key feature of ET (Jun & Steinberg 2009, 2017). The decays are characterized by a flat region at $f/f_{\text{vor}} < 1$ and by the steep power law decay at $f/f_{\text{vor}} > 1$ (see **Figure 1*d***), where f_{vor} is the main vortex frequency with a peak clearly visible at $f/f_{\text{vor}} = 1$ for all Wi and ϕ (Jun & Steinberg 2009, 2017). As revealed by the fits, the power spectrum decays scale as $E_{\Gamma\Gamma} \sim (f/f_{\text{vor}})^{-\mu}$ and $E_{pp} \sim (f/f_{\text{vor}})^{-\beta}$ for $\phi = 100$ ppm at various values of Wi and at the maximum Wi value for $\phi \leq 900$ ppm with the exponents $\mu \simeq 4$ and $\beta \simeq 3$ [see **Figure 1*d*,*e***] and Jun & Steinberg (2009, 2017)]. In the semidilute entangled range of $900 < \phi \leq 3{,}000$ ppm, $E_{\Gamma\Gamma}$ and E_{pp} decay with different exponents: $\mu \simeq 4.6$ and $\beta \simeq 2.2$, respectively (Jun & Steinberg 2009, 2017). Thus, there is another striking similarity with high-Re turbulence, but the exponents in ET are significantly larger.

The strong enhancement of mixing efficiency, one of the main features of ET (Groisman & Steinberg 2001b; Burghelea et al. 2004a,b), is directly related to the drastic increase of the transverse diffusion coefficient with Wi that is observed in a porous medium and caused by enhanced velocity fluctuations. This results in a strongly enhanced dispersion of micrometer-sized particles in a polymer solution flow in a porous medium in the ET regime (Scholz et al. 2014). Clarke et al. (2015), Howe et al. (2015), and Mitchell et al. (2016) also reported similar results of the strong particle dispersion above the well-defined threshold Wi_c in a polymer solution flow in both microfluidic devices and rock cores. The increase in particle dispersion, the apparent viscosity thickening, and the growth of the flow velocity fluctuations occur above the same Wi_c that causes the increase in oil displacement efficiency (anomalous desaturation) at $Wi > Wi_c$ in 3D

opaque porous structures (sandstone), phenomena that have important industrial applications in oil recovery (Clarke et al. 2015, Howe et al. 2015, Mitchell et al. 2016).

3.2. Microscopic Approach: Coil–Stretch Transition in a Polymer Conformation in a Random Flow

The discovery of ET has initiated theoretical and numerical studies on microscopic (molecular) and hydrodynamic levels. On the molecular level, the existence of ET is attributed to the occurrence of a coil–stretch transition (CST) in a polymer conformation in a fluctuating velocity field. As considered theoretically for a homogeneous, isotropic, and fluctuating velocity field at sufficiently low ϕ, polymers are stretched and advected by the flow with negligible back reaction on the flow (Balkovsky et al. 2000, Chertkov 2000, Chertkov et al. 2005, Turitsyn 2007). Thus, polymers are treated as passive objects, whose dynamics is governed by the equation based on the balance between polymer stretching by the velocity gradient tensor in a random flow with shear rate $\dot{\gamma}$ in the (x, y)-plane, $\nabla_j \mathbf{V}_i = \dot{\gamma}\delta_{ix}\delta_{jy} + \widetilde{\nabla_j \mathbf{V}_i}$, where $\widetilde{\nabla_j \mathbf{V}_i}$ is the random part of the velocity gradient tensor, and the relaxation in the approximation of the Oldroyd-B model is (Hinch 1977)

$$\partial_t \mathbf{R}_i = \mathbf{R}_j \nabla_j \mathbf{V}_i - \lambda^{-1}\mathbf{R}_i + \boldsymbol{\xi}_i. \qquad 1.$$

Here, $\mathbf{R}_i$ is the end-to-end vector for a given configuration of a polymer i, and $\boldsymbol{\xi}_i$ is the thermal Langevin force.

We consider two cases: (*a*) a random, homogeneous, isotropic flow, where both $\dot{\gamma}$ and $\boldsymbol{\xi}_i$ are neglected (Balkovsky et al. 2000, Chertkov 2000, Eckhardt et al. 2002, Boffetta et al. 2003, Thiffeault 2003, Gerashchenko et al. 2005, Liu & Steinberg 2010a), and (*b*) a random flow with a strong shear component, where $\boldsymbol{\xi}_i$ is neglected (Chertkov et al. 2005, Turitsyn 2007, Liu & Steinberg 2010b). The former case (*a*) was first studied by Lumley (1972), who pointed out that $\widetilde{\nabla_j \mathbf{V}_i}$ always has an elongation direction, although this direction fluctuates in space and time. Moreover, Lumley (1972) made the conclusion that there is a critical maximum eigenvalue of the strain rate tensor of the random velocity field normalized by λ, above which polymers can be stretched. However, the opposite assertion has also been considered (de Gennes 1986). The long-standing arguments over whether the CST takes place in a random flow were finally resolved experimentally on the hydrodynamic level by Groisman & Steinberg (2001a), who first showed evidence of a significant polymer stretching in ET. However, the main progress has been made by a formulation of the relation between the statistics of polymer stretching in a random flow and the stretching rate, that is, the maximum Lyapunov exponent Ψ of a random flow, which is the average logarithmic divergence rate of nearby Lagrangian trajectories in the flow (Balkovsky et al. 2000, Chertkov 2000). Balkovsky et al. (2000) theory predicts a power law tail of a probability density function (PDF) of polymer extensions, $P(R_i) \propto R_i^{-\delta-1}$, where $\delta = \lambda^{-1} - \Psi$ in the vicinity of the CST at $R_i \gg R_0$, with $\delta > 0$ below the CST and $\delta < 0$ above it (Balkovsky et al. 2000), which has been confirmed by numerical simulations of 3D shear turbulence (Eckhardt et al. 2002) and of 2D turbulence (Boffetta et al. 2003). Positive δ corresponds to the majority of the polymers being in the coil state, whereas negative δ corresponds to the majority of the polymers being strongly stretched. Consequently, $P(R_i)$ is normalizable at $\delta > 0$, whereas at $\delta < 0$, polymer stretching is unbounded, i.e., PDFs of their extension become nonstationary, with all moments growing exponentially in time. Thus, the model with an infinite polymer extension is inadequate. This means that only accounting for the nonlinear polymer elasticity allows one to recover a stationary statistics at $\delta < 0$ above the CST. The abrupt change in the polymer extension statistics at $\delta = 0$ is interpreted as the CST in a random flow (Balkovsky et al. 2000, Chertkov 2000). It can be rewritten via the local Weissenberg

number $Wi_{\rm loc}$ in a random flow, defined via either the Lyapunov exponent or the rms (root mean square) of velocity gradient instead of Wi defined via the averaged velocity gradient, U/L. The superscript cst means that it corresponds to the CST onset value as $Wi_{\rm loc}^{\rm cst} \equiv \lambda\Psi \approx \lambda(\nabla\mathbf{V})_{\rm rms} = 1$, since Ψ is approximately $(\nabla\mathbf{V})_{\rm rms}$ in a random flow. For a random, homogeneous, and isotropic flow with zero correlation time, $P(R_i)$ has been derived explicitly for both the Oldroyd-B and finite extensibility nonlinear elasticity (FENE) models, and the result was obtained by direct computation (Balkovsky et al. 2000, Chertkov 2000, Thiffeault 2003, Celani et al. 2005, Afonso & Vincenzi 2005). It is now obvious that Wi defined via the average velocity U is irrelevant for the CST characterization.

Predictions of the CST onset and the PDFs of the polymer extensions were first verified experimentally using fluorescently labeled λ-DNA polymer molecules (Gerashchenko et al. 2005) and later using much longer T4 DNA molecules (Liu & Steinberg 2010a,b). In the latter, the statistics of polymer stretching was measured by tracking fluorescently labeled polymers in a random velocity field of ET in two cases: first, at a relatively low average shear rate and a velocity field rather close to homogeneous and isotropic, and second, as a function of shear rate. All three experiments (Gerashchenko et al. 2005; Liu & Steinberg 2010a,b) were conducted in a miniaturized version of a swirling flow between rotating and stationary disks, shown in **Figure 2*d***. To verify a dramatic change in the PDF of polymer stretching as a function of Wi, the researchers measured the polymer extensions in a 2D plane in which polymers were detected (see **Figure 2*a–c***), and in this way the CST onset was identified. The measurements of both the polymer stretching and the Lyapunov exponent, Ψ, of the velocity field were conducted in the same setup below and above the CST, using first λ-DNA and later T4 DNA molecules. In the latter, instead of the statistics of Ψ, $(\partial V_\theta/\partial r)_{\rm rms}$ was obtained via PIV (Liu & Steinberg 2010b). In this way, the value of the CST onsets, $Wi_{\rm loc}^{\rm cst} = 0.77 \pm 0.20$ for λ-DNA (Gerashchenko et al. 2005) and $Wi_{\rm loc}^{\rm cst} = 0.70 \pm 0.2$ for T4 DNA (Liu & Steinberg 2010b, 2014), were obtained in two experiments, in good agreement with predictions (Balkovsky et al. 2000). The value was also investigated by direct numerical simulation (DNS) for the Oldroyd-B (Eckhardt et al. 2002, Boffetta et al. 2003, Celani et al. 2005) and FENE models (Afonso & Vincenzi 2005, Davoudi & Schumacher 2006, Bagheri et al. 2012), as well as for multibead chains (Watanabe & Gotoh 2010). PDFs of polymers with the finite maximum extension, $R_{\rm max} < \infty$, show a stationary shape at $Wi_{\rm loc}^{\rm cst} > 1$, where $R_{\rm max}$ is the polymer full extension length. As $Wi_{\rm loc}^{\rm cst}$ increases, the peak of $P(R_i/R_{\rm max})$ moves from $R_0/R_{\rm max}$, where R_0 is the gyration radius, toward values close to unity with only one peak in each PDF for a given Wi, as observed in experiments (see **Figure 2**) (Gerashchenko et al. 2005; Liu & Steinberg 2010a,b, 2014) and numerical simulations with a short Lagrangian correlation time of the velocity field, $\tau_{\rm corr}$ (Afonso & Vincenzi 2005, Davoudi & Schumacher 2006, Watanabe & Gotoh 2010, Bagheri et al. 2012).

However, in a random flow an additional control parameter, the Kubo number $Ku = \tau_{\rm corr}\Psi$, where $\tau_{\rm corr}$ is the velocity correlation time, may affect the dynamics and deformations of polymers and so the shape of their PDF, as shown theoretically and numerically by Musacchio & Vincenzi (2011). The case where the correlation time is close to zero, and so $Ku \simeq 0$, is reviewed above. At large Ku, the appearance of the stretched state occurs when the PDF maximum decreases at $R \approx R_0$ and a second maximum simultaneously emerges close to $R_{\rm max}$ (Musacchio & Vincenzi 2011), in sharp contrast to the uncorrelated isotropic flow. Our recent measurements provide $\tau_{\rm corr} \approx 0.5$ s or less and $\Psi \approx (\nabla\mathbf{V})_{\rm rms} \simeq \lambda^{-1}\ {\rm s}^{-1}$ for $Wi_{\rm loc} = \lambda(\nabla\mathbf{V})_{\rm rms} \approx 1$ in the ET regime of a serpentine channel flow, which gives $Ku \ll 1$ (Afik & Steinberg 2017). Moreover, $\tau_{\rm corr}$ obtained from the velocity autocorrelation function in time is more than two orders of magnitude smaller than λ [see figure 4*b* of Burghelea et al. (2004a) and supplemental figure 9SM of Jun & Steinberg (2017)].

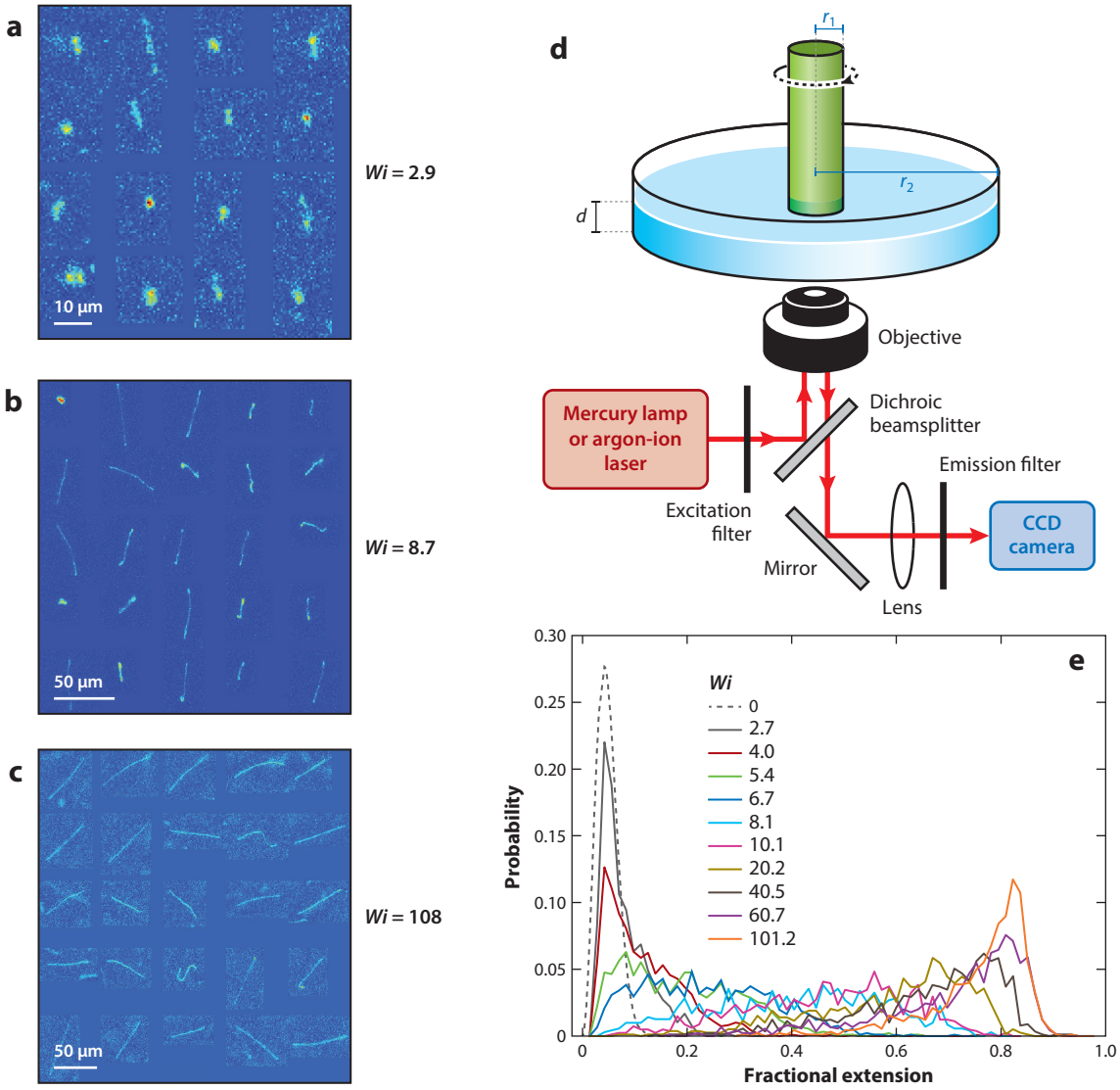

Figure 2

(*a–c*) Typical conformations of T4 DNA molecules (with a maximum extension length of $R_{max} \simeq 71.7$ μm) at various values of *Wi* in a polymer solution of concentration $c = 25.16$ μg/ml with 5% sucrose (DNA images are taken from different shots). (*d*) The setup for single-polymer stretching measurements in elastic turbulence. (*e*) PDFs of polymer extensions $P(x/R_{max})$ at $r_1 = 300$ μm and various values of *Wi*. Due to small r_1, which entails a small shear contribution at $Wi < Wi_{cst}$, the power law tails decay with $\delta > 0$, while at $Wi > Wi_{cst}$, one finds $\delta < 0$, where Wi_{cst} corresponds to the CST in the polymer conformation. Panels adapted with permission from (*a–c*) Liu & Steinberg (2014), (*d*) Gerashchenko et al. (2005), and (*e*) Liu & Steinberg (2010b, 2014). Abbreviations: CCD, charge-coupled device; CST, coil–stretch transition; PDF, probability density function.

The role of the increasing shear rate $\dot{\gamma}$ in the polymer stretching and angular orientation statistics in ET was elucidated by Liu & Steinberg (2010b). As the steady component of the shear-rate, $\dot{\gamma}$, becomes stronger, the polymer stretching becomes less efficient and the polymer alignment with the shear direction becomes more effective, where the direction is defined by the out-of-the-shear-plane inclination angle θ (figure 6 of Liu & Steinberg 2010b). These results were obtained

by taking measurements at three radial locations $r_1 < r_2 < r_3$ in the swirling flow at ET with $\dot{\gamma} \sim r$ (Liu & Steinberg 2010b, figure 6 for polymer stretching and figures 5–7 for θ), in good accord with theory and simulations for high $\dot{\gamma}$ (Chertkov et al. 2005, Davoudi & Schumacher 2006, Turitsyn 2007) and in contrast to the random PDF of θ in ET at low $\dot{\gamma}$ (figure 8 of Liu & Steinberg 2010b). The most intriguing result found above the CST is the limiting slope of the PDF of the polymer extension tail with an exponent of about −4.5 at the highest $Wi = \lambda(\partial V_\theta/\partial r)_{\rm rms}$ and low $\dot{\gamma}$. This is not seen in **Figure 2*e***, since the results are presented in linear scales [see figure 6 of Liu & Steinberg (2010b), where the results are shown in log-log scales].

3.3. Macroscopic Approach: Theory and Numerical Simulations of Elastic Turbulence

In this section, I discuss the theory of elastic turbulence, its assumptions and predictions, further developments of the scaling approach for deriving a relation between different scaling exponents, and a detailed comparison of theory with numerical simulations and experimental results.

3.3.1. Theory of elastic turbulence. The CST has a remarkable macroscopic consequence on a flow: At $Wi_{\rm loc} > 1$, a polymer solution above the CST essentially becomes a non-Newtonian fluid, and at sufficiently large $Wi_{\rm loc} > Wi_{\rm loc}^{\rm cst}$, the flow starts to be chaotic. On a hydrodynamic level, theory (Balkovsky et al. 2001, Fouxon & Lebedev 2003) and numerical simulations (Berti et al. 2008, Berti & Boffetta 2010) of ET were developed for an unbounded, isotropic, homogeneous flow of a dilute polymer solution described by the Oldroyd-B model (Bird et al. 1987). The theory of ET is based on the Navier–Stokes equation for a polymer solution with a coupling term, arising from the back reaction of the elastic stress field σ_{ij} generated by stretched polymers on the velocity field V_i, and the equation for σ_{ij} in the Oldroyd-B model approximation (Bird et al. 1987). For ET at $Re \ll 1$, the inertial terms in the Navier–Stokes equation can be neglected compared with elastic term. For the sufficiently stretched polymers, $R_0 \ll R_i \ll R_{\rm max}$, one gets $\sigma_{ij} \gg \sigma_{ij}^0$, where σ_{ij}^0 is the elastic stress due to thermal noise. Then the properties of polymer stress tensor σ_{ij} are established using the Lagrangian description of a fluid flow (Fouxon & Lebedev 2003). In a statistically steady state realized at time much larger than the velocity gradient correlation time the elastic stress tensor is uniaxial $\sigma_{ij} = B_i B_j$. Indeed, at $R \gg R_0$, the contribution of thermal fluctuations into σ_{ij} becomes negligible, so that $\sigma_{ij} \sim R_i R_j$ holds. The uniaxial form of σ_{ij} allows for rewriting the set of equations for polymer hydrodynamics in a form similar to the MHD equations with $\sigma_{ij} = B_i B_j$ but with an important difference, namely, dissipation due to relaxation instead of a magnetic resistivity (Landau & Lifschitz 1989):

$$\nabla p/\rho = (\mathbf{B}\nabla)\mathbf{B} + (\eta/\rho)\triangle\mathbf{V}, \qquad \nabla \cdot \mathbf{V} = 0, \qquad 2.$$

$$\partial_t \mathbf{B} + (\mathbf{V}\nabla)\mathbf{B} = (\mathbf{B}\nabla)\mathbf{V} - \mathbf{B}/\lambda, \qquad \nabla \cdot \mathbf{B} = 0, \qquad 3.$$

where **B** is the solenoidal vector, which characterizes the direction and the strength of the coherent polymer extension. It is defined up to a sign, and in a contrast to the magnetic field vector in MHD, it is the director, analogously to the director in nematics (Fouxon & Lebedev 2003). At sufficiently large elastic stress back reaction due to the term $(\mathbf{B}\nabla)\mathbf{B}$, the flow reaches a chaotic, statistically steady state defined as ET.

Thus, the hydrodynamic description of the polymer solution velocity field and the dynamics of the elastic stress for linear polymers given by Equations 2 and 3 are analogous to the description of a small-scale viscosity-dominated dynamo in MHD (Landau & Lifschitz 1989) and turbulent

advection of a passive scalar in the Batchelor regime (Batchelor 1959, Fouxon & Lebedev 2003), although there are some significant differences between them. The random stretching of the frozen-in magnetic field lines by an advecting random velocity field is similar to polymer stretching in ET, but the relaxation term replaces the diffusion term in MHD, whereas in the passive scalar advection problem the key dynamo effect is absent. However, in all three cases the basic physical mechanism is the same and is directly related to the classical Batchelor regime of mixing, namely, stretching and folding of a fluid parcel by an advecting randomly fluctuating velocity field that, in the case of ET, results in deformations of the elastic stress field. This mechanism of small scales generation leads to the algebraic power spectrum decay of the elastic stress and velocity in ET, as well as the passive scalar in the Batchelor regime of inertial turbulence and the magnetic field in MHD.

3.3.2. Assumptions and predictions of theory. The main result of the theory is based on the following two assumptions. The first assumption is that a statistically stationary state of the velocity field occurs due to the back reaction of stretched polymers on the flow. It means that the maximum Lyapunov exponent Ψ of ET, and $(\nabla_i V_j)_{\rm rms}$, defining the polymer stretching rate is on the order of λ^{-1}. The equality of Ψ and λ^{-1} leads to the criterion of the CST onset, $Wi_{\rm loc} \simeq 1$, and correspondingly to a saturation of σ_{ij} and $(\partial V_i/\partial x_j)_{\rm rms}$ even for linear polymer elasticity. Since polymers with linear elasticity are stretched indefinitely at larger $Wi_{\rm loc}$ and the PDF of the polymer extensions becomes nonstationary, this equality also remains valid in ET. The second assumption is that both viscous $\eta(\nabla_i V_j)^2$ and stress relaxation σ_{ij}/λ mechanisms are of the same order in their contribution to the energy dissipation, which provides $\sigma\lambda/\eta \approx Wi^2_{\rm loc}$. As a result, both assumptions give the saturated value of the elastic stress in ET, namely $\sigma\lambda/\eta \approx 1$, a quantitative prediction, which should be tested in both micro- and macroscopic experiments.

However, the major result of the theory is the prediction of the power law decays of the kinetic energy spectrum, $E(k) \sim V^2\rho L(kL)^{-\alpha}$, with $\alpha > 3$, and the elastic energy spectrum, $E_B(k) \sim B^2 L(kL)^{-\nu}$, with $\nu = (\alpha - 2) > 1$(Fouxon & Lebedev 2003), which is close to the passive scalar Batchelor decay exponent, -1 (Batchelor 1959). The exponents of both power spectrum decays are obtained by applying a passive scalar approach to a description of the small-scale perturbations of the velocity $\acute{\mathbf{V}}$ and elastic stress $\acute{\mathbf{B}}$ fields passively advected by the large-scale random velocity $\mathbf{V}$ field, where one has $\acute{\mathbf{V}}, \acute{\mathbf{B}} \ll \mathbf{V}, \mathbf{B}$ and $\nabla\acute{\mathbf{V}} \ll \nabla\mathbf{V}$ while $\nabla\acute{\mathbf{B}} \sim \nabla\mathbf{B}$ (Fouxon & Lebedev 2003). From both power spectrum expressions, one finds that the main energy in ET is carried out by the stretched polymers. The latter follows from $E(k) \sim Re(kL)^{-2}E_B(k)$, where $\rho(V/B)^2 \sim Re \ll 1$. The latter follows from $B^2 \sim \eta/\lambda$ and $\rho V^2 \sim \rho(L/\lambda)^2$, which leads to $\rho(V/B)^2 \sim L^2\rho/\lambda\eta = Re/Wi \sim Re$ at $Wi \gg 1$. The value of α mentioned above is in good agreement with experimental results (Groisman & Steinberg 2000, 2001b, 2004; Burghelea et al. 2007; Varshney & Steinberg 2018b), whereas the elastic energy spectrum scaling is difficult to verify experimentally, although it has been tested numerically at moderate Re below the dissipation scale (Nguyen et al. 2016). In this regime, the polymer energy spectrum is found to be described by a power law decay k^{-2}, i.e., $\nu \approx 2$, which is different from the theoretical prediction of $\nu > 1$, although it does not contradict it. The same relation between ν and α in ET can also be obtained by scaling arguments (Steinberg 2019). Taking into account that $R_i \sim \nabla\mathbf{V}$ followed from the Oldroyd-B model, one finally obtains $E_B(f) = \langle BB\rangle_f \sim f^{-\nu} \sim \langle\nabla\mathbf{V}\nabla\mathbf{V}\rangle_f \sim f^{-(\alpha-2)}$, since one finds $E(f) = \langle VV\rangle_f \sim f^{-\alpha}$, resulting in the equality $\nu = \alpha - 2$, equivalent to the relation obtained by Fouxon & Lebedev (2003) via analytical calculations, as discussed above.

3.3.3. Derivation of the scaling relation in elastic turbulence. Although the theory of ET predicts the first relation between the scaling exponents of the elastic and kinetic energy spectrum decays, $\nu = \alpha - 2$ (Fouxon & Lebedev 2003), it does not provide any clue about the relation

between the scaling exponents of the velocity $E(f) \sim f^{-\alpha}$ and pressure $E_{pp}(f) \sim f^{-\beta}$ power spectrum decays, α and β. Using Equation 2, one derives the relation between the Fourier transforms of the pressure $E_p(k)$, velocity $E_u(k)$, and the elastic stress $E_B(k)$ in ET (Steinberg 2019):

$$ikLB^2L^{\alpha-1}(kL)^{-(\alpha-2)} = ipkL(kL)^{-\beta/2} + \eta kLVL^{-1}(kL)^{-(\alpha-2)/2}. \quad 4.$$

One can demonstrate that the first term on the left-hand side of Equation 4 is the Fourier transform of the divergent part of the elastic stress, $\sigma_{ij}^{\text{div}} = (B_iB_j)^{\text{div}}$. Indeed, straightforward transformation of Equation 2 leads to the equation $\Delta p = \partial^2(B_iB_j)^{\text{div}}/\partial x_i \partial x_j$ (Jun & Steinberg 2009, 2017; Steinberg 2019), whose Fourier transform provides the relation $E_B(kL)^{\text{div}} \sim E_p(kL) \sim p(kL)^{-\beta/2}$. Similar considerations lead to the exact relation between the vortical (divergent-free) part of the elastic stress, $\sigma_{ij}^{\text{curl}} = (B_iB_j)^{\text{div}}$, and the vorticity, $\mathbf{\Omega} \equiv \nabla \times \mathbf{V}$, from the same Equation 2 (Jun & Steinberg 2017, Steinberg 2019), namely, $\nabla(\mathbf{BB})^{\text{curl}} = -(\eta/\rho)\Delta\mathbf{\Omega}$. Then, its Fourier transform results in the relation $E_B(kl)^{\text{curl}} \sim \eta VL^{-1}(kL)^{-(\alpha-2)/2}$. Thus, Equation 4 can be rewritten as $E_B(kL) = E_B(kL)^{\text{div}} + E_B(kL)^{\text{curl}}$, which after straightforward algebraic transformations results in the following algebraic equation:

$$B^2x^2 = px^{\beta/(\alpha-2)} - i(\eta V/L)x, \quad 5.$$

with $x = (kL)^{-(\alpha-2)/2}$. At $kL < 1$, where both the elastic and kinetic energy spectra in ET are flat, one gets $x > 1$. Then the last term in Equation 5 corresponding to $E_B(kL)^{\text{curl}}$ can be neglected due to $x > 1$ and $pL/V\eta \gg 1$, the ratio of the coefficients of two terms on the right side of Equation 5. Moreover, even at $kL \geq 1$, for $x < 1$, in the decay range of $E_B(kL)$ in ET, one also finds $E_B(kL)^{\text{div}}/E_B(kL)^{\text{curl}} > 1$ at least up to $kL \approx 10$, in spite of the steeper decay of $E_B(kL)^{\text{div}}$ than of $E_B(kL)^{\text{curl}}$ at $kL \geq 1$. Thus, the last term in Equation 5 can be neglected in the whole range of the power law decay of $E_B(kL)$, since $E_B(kL)^{\text{div}}$ plays the dominant role in the elastic stress field, whereas $E_B(kL)^{\text{curl}}$ in ET makes a minor contribution. As a result, one obtains from Equation 5 a new scaling relation, $\beta = 2(\alpha - 2)$ (Steinberg 2019).

3.3.4. Comparison of theory with numerical simulations and experiment. In recent years, various numerical simulations verifying experimental and theoretical results in ET have been carried out in different flow geometries. First, 2D simulations were employed to test the power law decay exponent of the velocity power spectrum in ET in unbounded, periodic Kolmogorov shear flow (Berti et al. 2008, Berti & Boffetta 2010), in wall-bounded channel flow with a linear periodic array of obstacles (Grilli et al. 2013), and in TC flow geometries (van Buel et al. 2018) of a dilute polymer solution using the same Oldroyd-B model at low *Re*. All of these simulations found similar results of $\alpha > 3$ with variations between 3.2 and 4.3, in accord with experiment and theory. Moreover, other characteristic features of ET were verified, such as a sharp growth of the friction factor and efficient mixing (Berti et al. 2008, Berti & Boffetta 2010, Grilli et al. 2013). Another 2D DNS (Gupta & Pandit 2017) elucidated the nature of melting of a vortex crystal in a nonequilibrium, forced 2D fluid film of a polymer solution described by the FENE-Peterlin (FENE-P) nonlinear polymer model (Bird et al. 1987). For $Re \ll 1$ and $Wi \gg 1$, this melting is induced by a chaotic flow that is characterized by the decay of the kinetic energy spectrum in a k-domain with $\alpha \approx 3.2$ (Gupta & Pandit 2017), in reasonable agreement with experiments (Groisman & Steinberg 2000, 2001b).

Using the FENE-P model, Thomas et al. (2006, 2009) conducted elaborate 3D DNS of highly inhomogeneous, anisotropic, time-dependent, and wall-bounded TC flow of a dilute polymer solution at intermediate *El*. At sufficiently high *Wi*, the power spectra of the radial and axial velocities revealed the power law decay with $\alpha \approx 3$ in the range of DOs that corresponds to ET but with the

influence of inertia (Groisman & Steinberg 1998b, 2004; Thomas et al. 2009). Later on, Liu & Khomami (2013) used the same DNS approach to characterize ET in the TC flow of a viscoelastic fluid with $El \leq 5$ by generating PDFs and radial velocity V_r frequency power spectra, $E_{V_r}(f)$. Specifically, $E_{V_r}(f)$ taken at the middle of the gap accurately reproduced the experimentally measured two regions of the power law decays with the exponents -1.1 and -2.2 in the low- and high-f regions, respectively, in spite of the difference in the Reynolds number: $Re \sim 10$ in the simulation and $Re < 1$ in the experiment. However, the shapes of PDFs of V_r differed significantly: They were slightly skewed toward negative V_r in the experiment (Groisman & Steinberg 2004) and highly skewed toward negative V_r in the simulation (Liu & Khomami 2013). The latter resembles PDFs of DW, OS, and DO patterns at lower Wi and larger Re than those presented by Groisman & Steinberg (1998a), where the strong skewness was associated with a strong asymmetry between inflow and outflow. The key conclusion of DNS was the independence of the exponent value of the power law decay of the velocity power spectrum from the polymer model. However, the assumptions of the ET theory (Fouxon & Lebedev 2003) that led to the specific predictions of the saturation of $Wi_{\text{loc}} \approx 1$ as a function of Wi and to the limiting value of the elastic stress require further experimental and numerical tests.

There has been a separate observation of chaotic behavior of a viscoelastic fluid flow at low inertia and large elasticity in a low-dimensional shell model that mimics the interactions between the Fourier modes of the velocity field and the field of the stretched polymers (Ray & Vincenzi 2016). The shell model can be regarded as a reduced, low-dimensional version of the FENE model. In spite of the shell model's extreme simplicity, which contains no information about the spatial structure of both fields, it replicates the main features of ET, including the decay of the velocity power spectrum with $\alpha = -4$ and enhanced mixing due to the growth of the Lyapunov exponent values with Wi. Thus, the conclusion of the model is that the specific geometrical configuration of the system is not essential for ET, and that the physical mechanism leading to ET does not rely on the boundary conditions or the mean flow (Ray & Vincenzi 2016).

3.4. Small-Scale Dynamics in Viscoelastic Turbulence at $Re \gg 1$

Currently, there is significant evidence that elasticity qualitatively modifies the velocity power spectrum below the dissipation scale ζ in inertial turbulence due to a strong increase of energy content and a reduction in the energy dissipation rate at small scales below ζ due to a substantial flow of energy from stretched polymers toward the flow. Indeed, several 3D DNSs of homogeneous and isotropic hydrodynamic turbulence have found that the velocity power spectrum is modified at $k^{-1} < \zeta$ from an exponential decay for a Newtonian fluid to $k^{-\alpha}$ decay for a viscoelastic one. Therewith, in the inertial scale range, the kinetic energy spectrum remains roughly unchanged. The first evidence of this change at $k^{-1} < \zeta$ in isotropic decaying turbulence of a polymer solution was the observation of $\alpha \approx 4.2$–4.6, which is close to the ET values [see figure 30a of Watanabe & Gotoh (2013) and figures 5 and 6 of Watanabe & Gotoh (2014)]. A similar observation was made by DNS in EIT occurring in a pipe flow of a dilute polymer solution for the maximum drag reduction asymptote state (Dubief et al. 2013). EIT is a TDR regime of inhomogeneous and anisotropic inertially dominated turbulence in a pipe flow at $Re > 1{,}000$ (Samanta et al. 2013). In the intermediate scale range of EIT, between the inertial range with the Kolmogorov scaling exponent $-5/3$ and ζ, the power law scaling exponent α roughly between 11/3 and 14/3 was found, which is sufficiently close to the values reported by Watanabe & Gotoh (2013, 2014) and in ET. Another DNS carried out at weak El and moderate Re at $k^{-1} < \zeta$ reported $\alpha \approx 3.5$, very close to the ET values (Perlekar et al. 2010, Gupta & Pandit 2017). An interesting observation of the pressure power spectrum at $k^{-1} < \zeta$ revealed the decay exponent

$\beta = -3 \pm 0.2$ (Watanabe & Gotoh 2014) and $\nu = 2$ for the elastic energy spectrum in the same scale range. The latter was also observed in simulations by Nguyen et al. (2016) and De Angelis et al. (2012).

4. ELASTIC WAVES IN ELASTIC TURBULENCE

The important consequence of the similarity of Equation 3 to the MHD equations (Landau & Lifschitz 1989) is the existence of elastic waves similar to Alfvén waves in the presence of a large-scale magnetic field in MHD (Landau & Lifschitz 1989). Balkovsky et al. (2001) suggested the possibility of observing the elastic waves at small scales in TDR, where they can play a key role in modifying the velocity spectrum between the inertial and dissipation range of scales. By analogy with Alfvén waves in MHD, one gets the elastic wave linear dispersion relation as $\omega = (\mathbf{k} \cdot \hat{\mathbf{n}})[\mathrm{tr}(\boldsymbol{\sigma}_{ij})/\rho]^{1/2}$ with the elastic wave speed $c_{\mathrm{el}} = [\mathrm{tr}(\boldsymbol{\sigma}_{ij})/\rho]^{1/2}$, where ω and $\mathbf{k}$ are the rotation frequency and wave vector of the elastic waves, respectively, and $\hat{\mathbf{n}}$ is the major stretching direction vector, similar to the director used in nematics (Balkovsky et al. 2001). However, this evident difference between the elastic stress characterized by the director and the vector of the magnetic field does not alter the similarity between the elastic and Alfvén waves, since only uniaxial stretching is a necessary condition for the wave existence, with its speed determined by the stress value (Balkovsky et al. 2001). However, according to Fouxon & Lebedev (2003), the elastic waves should strongly attenuate in ET in the wave number range of the power law decay of the velocity power spectrum and so probably cannot be detected.

I would like to point out here that the elastic waves predicted to exist in viscoelastic fluid flows distinctly differ from so-called shear waves actively investigated both theoretically and experimentally in the 1980s–1990s (Joseph et al. 1986a,b; Joseph 1990). First, the shear waves generated by impulsive perturbations of a stationary viscoelastic fluid relax back into a rest state. This means that polymers in a coil state do not generate elastic stress in the resting solution. Moreover, they cannot also be stretched significantly, as they are perturbed on a timescale many orders of magnitude shorter than λ. Thus, on this timescale (high frequencies), in both Newtonian and non-Newtonian fluids, only fast shear waves may be excited, which are crucially different from the elastic waves discussed here. Indeed, the shear wave speed can be observed in any fluid, and it is defined by an expression similar to that presented above for the elastic wave speed, c_{el}. The key difference is in the effective rigidity determined by the storage modulus, which is much larger at the very high frequencies used for shear waves versus the much lower frequencies relevant to elastic waves. Although these waves are formally similar, they differ by orders of magnitude in their speeds.

A simple physical explanation of both Alfvén and elastic waves can be drawn from an analogy between the response of either magnetic or elastic tension on transverse perturbations and that of an elastic string when plucked. Thus, either Alfvén or elastic waves are transverse to the propagation direction, unlike longitudinal sound waves in plasma, gas, and fluid media (Landau & Lifschitz 1987). Moreover, c_{el} provides unique information about the elastic stress, whereas the wave amplitude is proportional to the transverse stress perturbations (Balkovsky et al. 2001).

The first evidence of elastic waves was obtained recently in ET of a dilute polymer solution flow in a wake between two widely spaced obstacles hindering a channel flow, the distinctive feature of which is the 2D nature of the ET flow in the midplane of the device, in contrast to other studied flow geometries (Varshney & Steinberg 2018b). In the low-frequency range, oscillations of the transverse flow velocity component V_y are observed (**Figure 3*a***). They are located below the frequency range of algebraic decay of the velocity power spectrum with $\alpha \simeq 3.4$, typical for ET (see **Figure 3*c***). The frequency peaks at low frequencies fall exponentially with increasing λf for five values of Wi and collapse by scaling them with $f_{\mathrm{d}}(Wi)$ as $E_{V_y}(f) \sim \exp(-f/f_{\mathrm{d}})$ [see **Figure 3*a*,*b*** and the inset in **Figure 3*b*** for $f_{\mathrm{d}}(Wi)$], where $f_{\mathrm{d}}(Wi)$ is the slope of the exponential

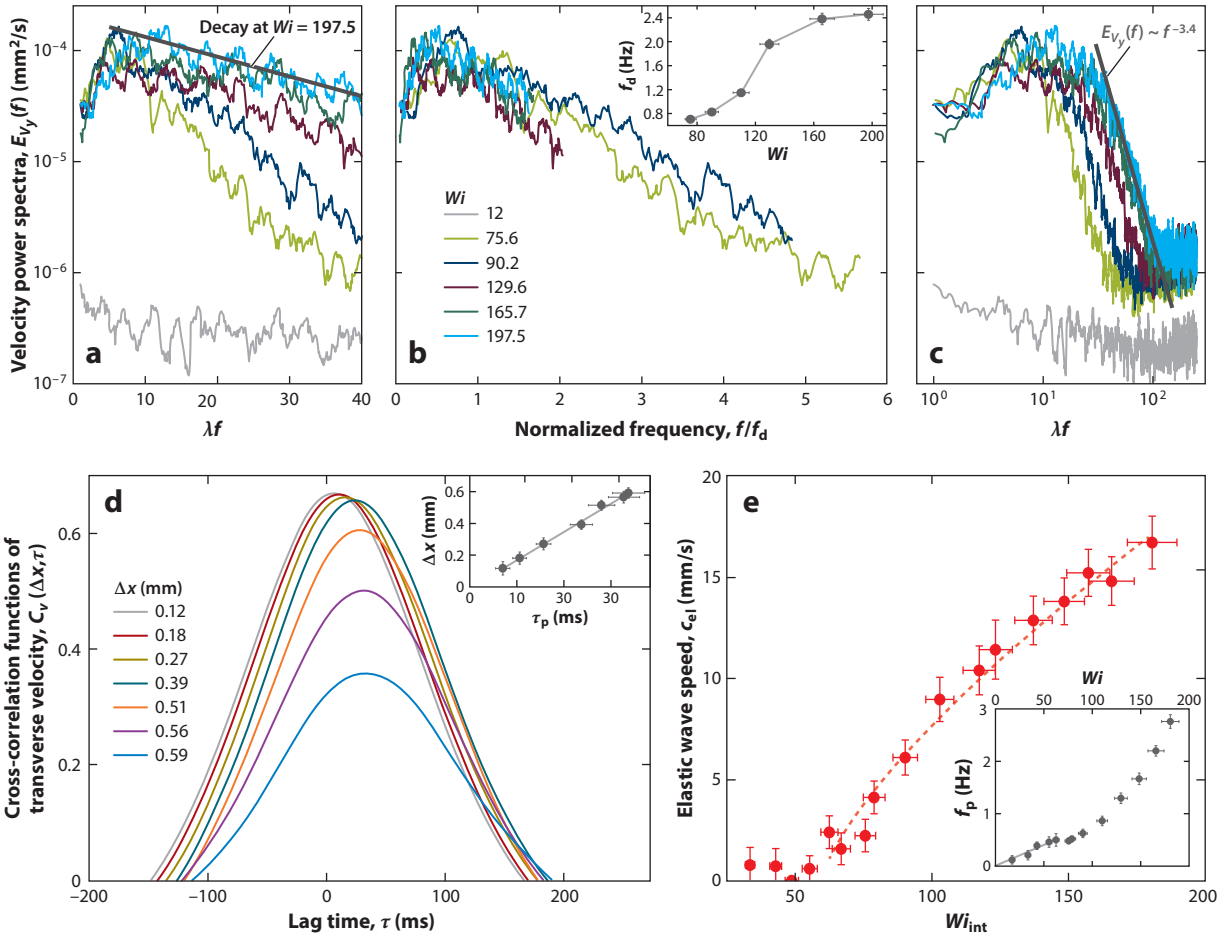

Figure 3

(*a*) Cross-stream velocity power spectra $E_{V_y}(f)$ in log-linear coordinates at low frequencies $\lambda f \leq 40$ in the ET regime for different values of *Wi*, where λ is the longest polymer relaxation time. The solid gray line indicates the exponential decay for $Wi = 197.5$ (*cyan line*). (*b*) $E_{V_y}(f)$ for different *Wi* collapse onto each other upon normalization of *f* by f_d, where $f_d(Wi)$ is the slope of the exponential decay of the velocity power spectra (*inset*). (*c*) $E_{V_y}(f)$ in log-log coordinates, for different *Wi*. The power law decay at high frequencies, $\sim 10 < \lambda f \leq 100$, is indicated by the fit with the exponent $\alpha_f \simeq -3.4 \pm 0.1$, typical to the ET regime. The spectra are obtained at $(x/R, y/R) = (5.2, 0.56)$, where *R* is the obstacle radius, which is close to the downstream obstacle and the center of the upper large vortex. $E_{V_y}(f)$ of steady flow is shown by gray lines in panels *a* and *c*. (*d*) Cross-correlation functions of the transverse velocity $C_v(\Delta x, \tau)$ versus the lag time τ for different values of Δ*x* obtained at $y/R = 0.18$ and for $Wi = 148.4$. (*Inset*) Δ*x* versus the time shift τ_p of the peak of $C_v(\Delta x, \tau)$ for $Wi = 148.4$; the slope of the linear fit (*solid line*) provides the elastic wave speed, c_{el}. (*e*) Dependence of c_{el} on Wi_{int}, where Wi_{int} is defined via the time-averaged shear rate of the cross-stream velocity in the interobstacle region. The dashed line is a fit, $c_{el} = A(Wi_{int} - Wi^c_{int})^\varepsilon$, given $A = 8.9 \pm 1.2$ mm s^{-1}, $\varepsilon = 0.73 \pm 0.12$, and the onset value $Wi^c_{int} = 1.75 \pm 0.2$. (*Inset*) Dependence of oscillations peak frequency f_p, shown in panels *a*–*c*, on *Wi*. The solid line is a linear fit to the data above the elastic instability. Figure adapted with permission from Varshney & Steinberg (2019).

decay of the velocity power spectra. The peak frequencies f_p depend linearly on *Wi*, at values just above the Hopf bifurcation (Varshney & Steinberg 2017), and after a short transition region, the dependence becomes nonlinear at $Wi \geq 60$ in the ET regime (**Figure 3*e***, inset). The central finding in the experimental proof of the existence of elastic waves is a power law dependence of c_{el} on *Wi* (**Figure 3*e***), which is obtained via the time shift τ_p of the peak of the temporal

cross-correlation function $C_v(\Delta x, \tau)$ between two spatially separated points Δx located on a horizontal line for each Wi (see **Figure 3*d*** and inset). The observed dependence of c_{el} on Wi deviates from the linear one predicted by the theory based on the Oldroyd-B model (Balkovsky et al. 2001, Varshney & Steinberg 2019). The onset of the elastic waves is found at $Wi_c = 59.7 \pm 1.8$, which coincides with the ET onset (Varshney & Steinberg 2018a). In light of the theoretical predictions (Fouxon & Lebedev 2003), it is surprising to observe the elastic waves in ET due to their anticipated strong attenuation. First, they are found outside the ET frequency range, in the low-f range. Second, the frequency range of the power law decay is shifted, by at least an order of magnitude, to values higher than those without the elastic waves, probably due to an additional energy flux caused by the elastic waves. Third, the estimates show that the k-region of the elastic waves is close to a low-attenuation window (Varshney & Steinberg 2019). Finally, an estimation of the elastic stress, based on maximal c_{el} reached in the experiment, gives $\langle\sigma\rangle = c_{el}^2\rho = 0.37$ Pa, which is lower than but comparable to the value $\langle\sigma\rangle \approx 1$ Pa obtained from the experiment on the stretching of a single T4 DNA polymer at similar concentrations (Liu & Steinberg 2010a), and it is orders of magnitude higher than the saturated value obtained from the theory assumptions (Fouxon & Lebedev 2003).

5. WALL-DOMINATED ELASTIC TURBULENCE: MACROSCOPIC APPROACH

The theory reviewed above and numerical simulations of statistically homogeneous, isotropic, and unbounded ET flow of a dilute polymer solution consider the simplest realization of elastically driven chaotic flows that can probably be found in a central region of a swirling flow. Obviously, such a random flow is significantly distinguished from the wall-bounded, inhomogeneous, and anisotropic flows studied experimentally. The ET regime in such flows is extensively studied experimentally in two flow geometries: (*a*) at 80 ppm of a PAM solution in both a swirling flow between rotating and stationary disks and a serpentine channel flow (Groisman & Steinberg 2000, 2001b; Burghelea et al. 2006, 2007; Jun & Steinberg 2011), and (*b*) in a wide range of polymer concentrations up to 3,000 ppm in a swirling flow (Jun & Steinberg 2009, 2017). The experiments reveal a role of elastic stresses in ET due to the presence of walls in both flow geometries, as well as the following features of ET (Burghelea et al. 2006, 2007; Jun & Steinberg 2009, 2011, 2017).

First, the PDFs of the injected torque Γ and pressure p fluctuations in a swirling flow show skewness and exponential tails, both of which indicate intermittent statistical behavior over a wide range of Wi and ϕ. Both features occur due to random bursts of the excessive elastic stresses near the wall into the bulk. Despite different underlying mechanisms, the striking similarity in the statistical properties of Γ and p fluctuations in ET and high-Re turbulence suggests the universality in statistical properties of Γ and p in a wide class of nonequilibrium hydrodynamic systems (see **Figure 4**) (Jun & Steinberg 2017).

Second, experiments also disclose, due to the presence of the walls in both swirling and curvilinear channel flows, a nonuniform distribution in ET of the compensated and normalized average azimuthal velocity profiles in the vertical (z/d) direction, $\tilde{V}_\theta^*(z/d) = \tilde{V}_\theta(z/d) - \tilde{V}_\theta(1/2) - (z/d)\partial\tilde{V}_\theta/\partial(z/d)|_{1/2}$, with $\tilde{V}_\theta(z/d) = \langle V_\theta(z/d)\rangle/V_\theta^d$ and d the distance between the disks (**Figure 5**), as well of as its rms values $(V_\theta)_{rms}$ and of the rms values of the velocity gradients $(\partial V_\theta/\partial r)_{rms}$ (Burghelea et al. 2007; Jun & Steinberg 2011, 2017). The average velocity and its rms values near the driving disk grow with Wi (Burghelea et al. 2007), as does $(\partial V_\theta/\partial r)_{rms}$ near the vertical wall, presented as $Wi_{loc} = \lambda(\partial V_\theta/\partial r)_{rms}$, which is directly related to the elastic stress (**Figure 5**, upper inset). Experimentally, the boundary layer thickness w is defined either from a deviation from a linear dependence near the wall on $\langle V_\theta\rangle$ and its rms profile $(V_\theta)_{rms}$ (see **Figure 5**) or from the peak in the $(\partial V_\theta/\partial r)_{rms}$ profile (see **Figure 6*a*,*b***). Thus, w is a new length scale, found to be much

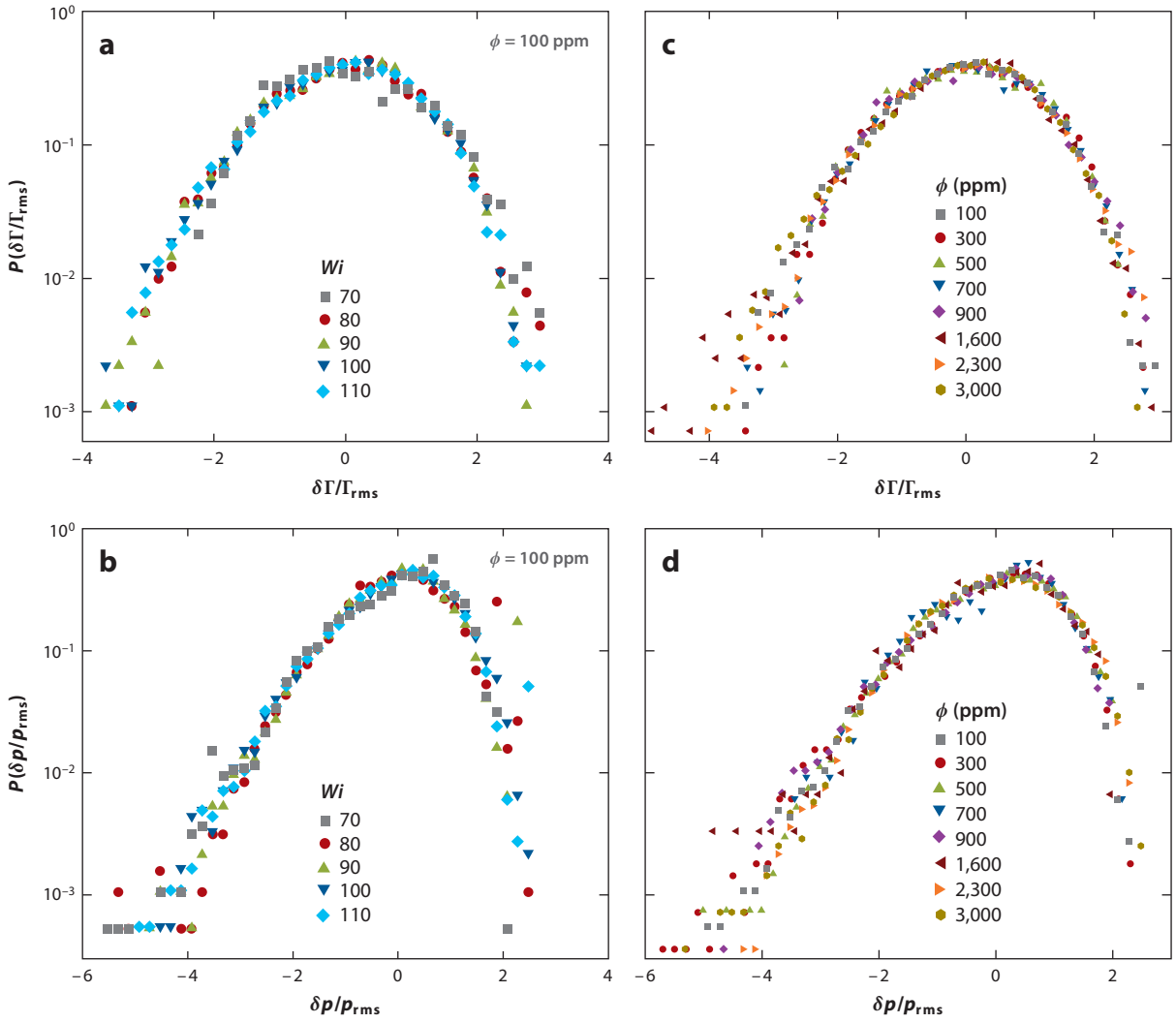

Figure 4

PDFs of fluctuations of (*a*) torque $\delta\Gamma/\Gamma_{rms}$ and (*b*) pressure $\delta p/p_{rms}$, scaled by their rms values, at different *Wi* for PAM solutions at $\phi = 100$ ppm. PDFs of (*c*) $\delta\Gamma/\Gamma_{rms}$ and (*d*) $\delta p/p_{rms}$ at maximum *Wi* for PAM solutions at different ϕ. Abbreviations: PAM, polyacrylamide; PDF, probability density function; rms, root mean square. Figure adapted with permission from Jun & Steinberg (2017).

smaller than the vessel size, independent of *Wi* (see **Figures 5** and **6*c***); w grows with η (**Figure 5**, bottom right inset) and reduces linearly with ϕ (**Figure 6*d***). The linear growth of $\langle V_\theta\rangle/(V_\theta)_{rms}$ with ϕ was observed by Jun & Steinberg (2017) and was found to be in agreement with theory (Belan et al. 2018). Similar spatial distributions of $\langle V_\theta\rangle$, $(V_\theta)_{rms}$, and $(\partial V_\theta/\partial r)_{rms}$ in the vicinity of lateral walls and w were also observed in curvilinear channel flow (Jun & Steinberg 2010, 2011). Thus, the $(\partial V_\theta/\partial r)_{rms}$ profile near the wall may reflect a spatial distribution of the elastic stresses. Contrary to the Kolmogorov dissipation scale and the related boundary layer width in inertial turbulence, the w scaling in ET does not follow from dimensional analysis.

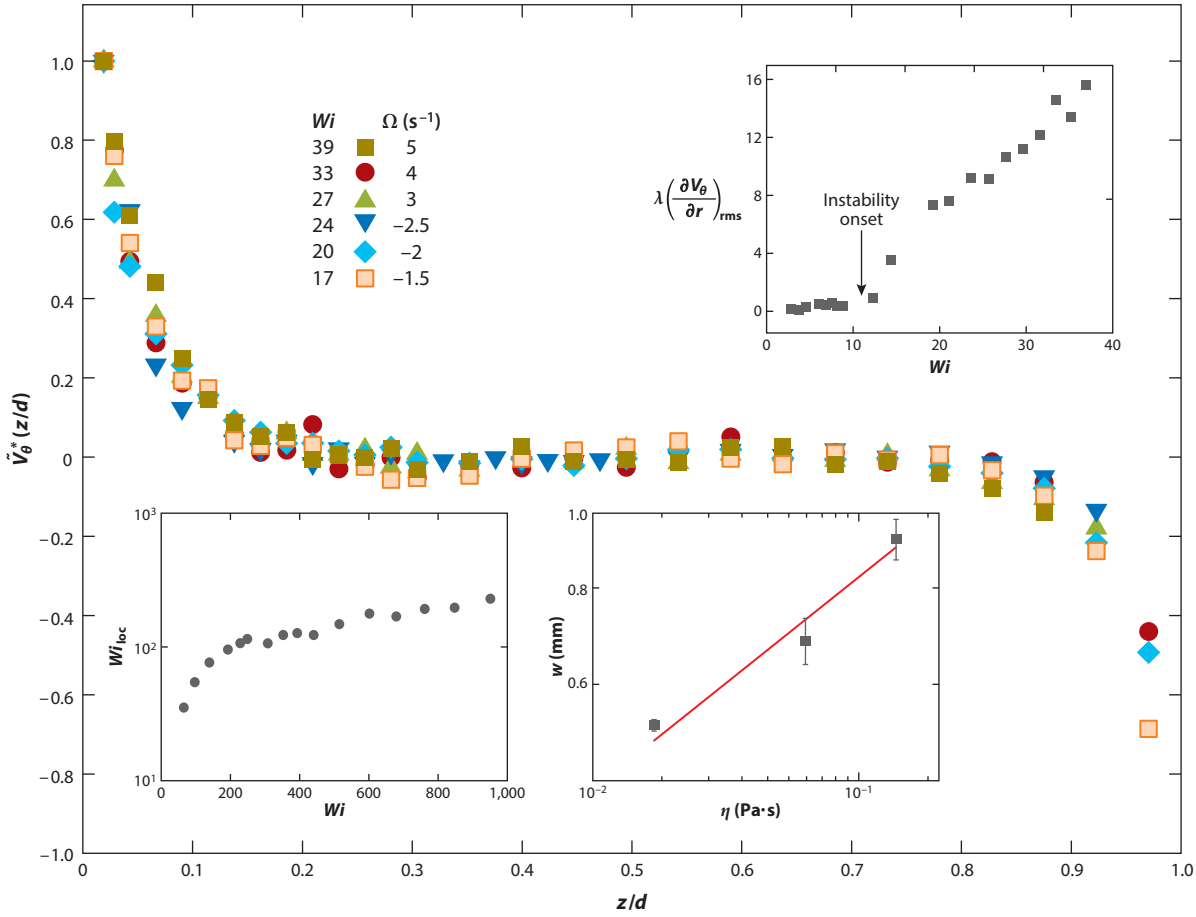

Figure 5

Compensated and normalized average azimuthal velocity vertical profiles $\tilde{V}_\theta^*(z/d)$ for several values of the vorticity Ω (or *Wi*) in swirling flow, where *d* is the gap between disks. (*Top inset*) Scaled root mean square (rms) of the velocity gradient in the boundary layer, $\lambda(\partial V_\theta/\partial r)_{\rm rms}$, versus *Wi*, where λ is the longest polymer relaxation time. The arrow indicates the onset of the primary elastic instability. (*Bottom right inset*) The boundary layer thickness *w* versus the solution viscosity *η*; the solid red line is the fit, $w \propto \eta^{0.26 \pm 0.05}$. (*Bottom left inset*) The local Weissenberg number $Wi_{\rm loc} = \lambda(\partial V_\theta/\partial r)_{\rm rms}$ averaged over r/d from 0.2 to 0.5 as a function of *Wi* for the curvilinear channel flow. Bottom left inset adapted with permission from Jun & Steinberg (2010); all other plots adapted with permission from Burghelea et al. (2006, 2007).

Third, in the boundary layer, $(\partial V_\theta/\partial r)_{\rm rms}$ reaches values up to one to two orders of magnitude larger than in the bulk [see **Figure 6*a*,*b*** for swirling flow and Jun & Steinberg (2011) for channel flow]. It has been suggested (Burghelea et al. 2007; Jun & Steinberg 2009, 2010) that the elastic stresses accumulate near the wall and are intermittently injected into the bulk, as indicated by the negative skewness and exponential tails in the PDFs of Γ and *p*. These jets of the elastic stress from the boundary layer introduce into the bulk small spatial scales on the order of $w \ll L$, breaking the flow smoothness on the vessel size. This intermittent injection of the elastic stresses (jets) is also supported by statistics of rare and strong drops in the Γ and *p* time series in ET in swirling flows (Burghelea et al. 2007; Jun & Steinberg 2009, 2010).

Fourth, the values of $Wi_{\rm loc}$ in a bulk flow grow strongly with *Wi* above the instability, but then they slow down in the ET regime and reach values up to 10–100, depending on the flow geometry

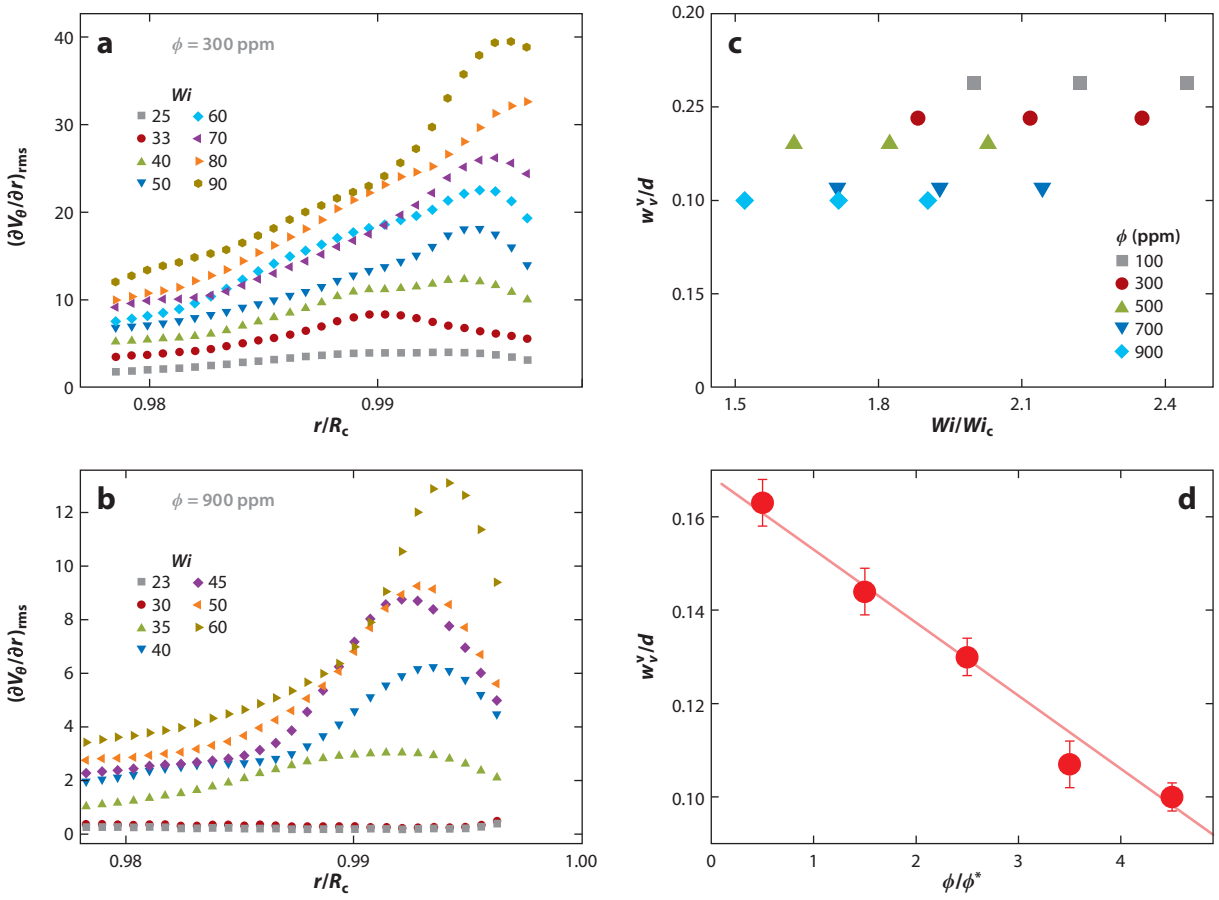

Figure 6

(*a*,*b*) The radial profiles of the root mean square (rms) azimuthal velocity gradients $(\partial V_\theta/\partial r)_{\rm rms}$ close to the side wall for various values of Wi and for two values of the polymer concentration ϕ, (*a*) 300 ppm and (*b*) 900 ppm, where R_c is the radius of the upper rotating disk. (*c*,*d*) The normalized vertical boundary layer width near the upper disk of the azimuthal velocity, w_v^v/d, plotted against (*c*) Wi/Wi_c for different ϕ and (*d*) ϕ/ϕ^* at the largest Wi, where Wi_c is the instability onset value and ϕ^* is the polymer overlapped concentration. The solid line is the linear fit $w_v^v/d = 0.17 - (0.016 \pm 0.001)\phi/\phi^*$, where superscript v means vertical and subscript v means the azimuthal velocity V_θ. Figure adapted with permission from Jun & Steinberg (2017).

(see **Figure 5**, bottom left inset, and **Figure 7*c*,*d***), which is much higher than the value $Wi_{\rm loc} \approx 1$ suggested by the basic assumptions (Balkovsky et al. 2001, Fouxon & Lebedev 2003).

Fifth, the velocity correlation time $\tau_{\rm corr}^{\rm v}$ and correlation length $r_{\rm corr}$ as functions of Wi and ϕ in ET are found from temporal $C_v(\tau)$ and spatial (radial) $C_v(r/d)$ correlation functions of $V_\theta(t, r)$ (see **Figure 7*a*,*b***). The corresponding $\tau_{\rm corr}^{\rm v}/\lambda$, obtained from the linear fits of $C_v(\tau)$ in log-linear coordinates (**Figure 7*a***, inset), decreases with Wi/Wi_c and is almost three orders of magnitude smaller than λ. Thus, the velocity field is close to δ-correlated in time, which agrees with $\tau_{\rm corr}^{\rm v}$ obtained in serpentine channel flow (see figure 4 of Burghelea et al. 2004a). The radial correlation functions of the azimuthal velocity $C_v(r/d)$ and the correlation length $r_{\rm corr}/R_c$ are found to be independent of Wi for all ϕ in swirling (see **Figure 7*b***) and curvilinear channel flows (Jun & Steinberg 2011). In the latter case, this means that the smoothness scale of the velocity

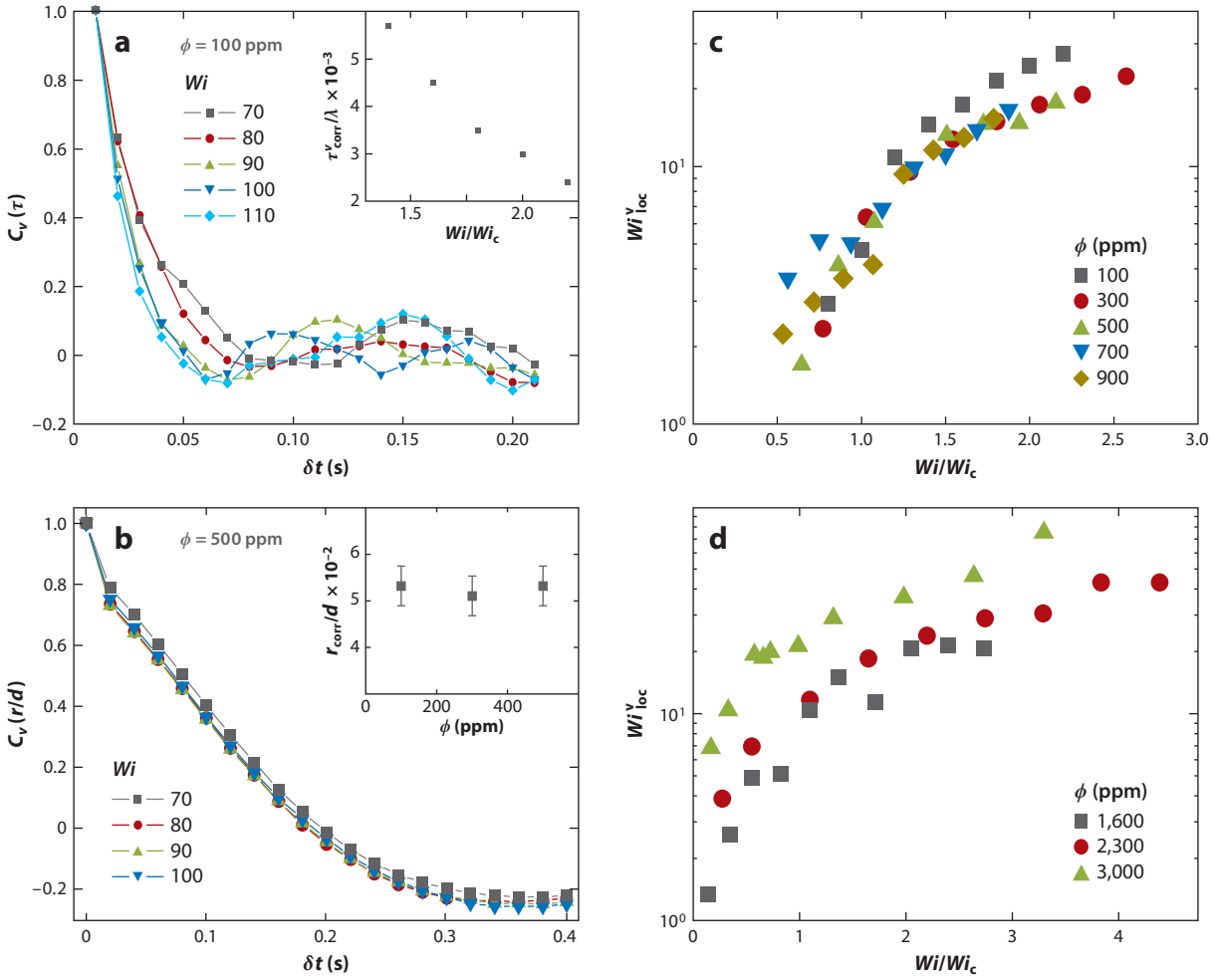

Figure 7

(*a*) Temporal correlation function of an azimuthal velocity in the horizontal plane $C_v(\tau)$ for five values of Wi and a polymer concentration of $\phi = 100$ ppm. (*Inset*) The velocity correlation time τ^v_{corr}/λ versus Wi/Wi_c, where Wi_c is the instability onset value. (*b*) Spatial correlation functions of an azimuthal velocity in the horizontal plane $C_v(r/d)$ for four values of Wi and $\phi = 500$ ppm. (*Inset*) The normalized velocity correlation length r_{corr}/d versus ϕ. The scaling of δr by R_c, which is more appropriate for the radial correlation function, gives $r_{corr}/R_c \simeq 0.054$, where r_{corr} is the correlation radius and R_c is the radius of the upper rotating disk. (*c*,*d*) The local Weissenberg number in the vertical plane, Wi^v_{loc}, based on the measurements in the vertical plane as a function of Wi/Wi_c for (*c*) five values of ϕ and (*d*) three high values of ϕ in the semidilute, entangled range. Figure adapted with permission from Jun & Steinberg (2017).

field in the bounded ET flow is on the order of $w \ll L$. The same conclusion has been made based on the Lagrangian approach to 3D velocity field measurements by the particle tracking method in ET (Afik & Steinberg 2017). Due to a surprising similarity in the scaling, statistics, and spatial distribution of the rms of the velocity gradients (or the elastic stresses) and passive scalar mixing in ET in the bounded container, below we discuss chaotic mixing in the Batchelor regime and the Lagrangian approach to measuring particle pair dispersion in ET.

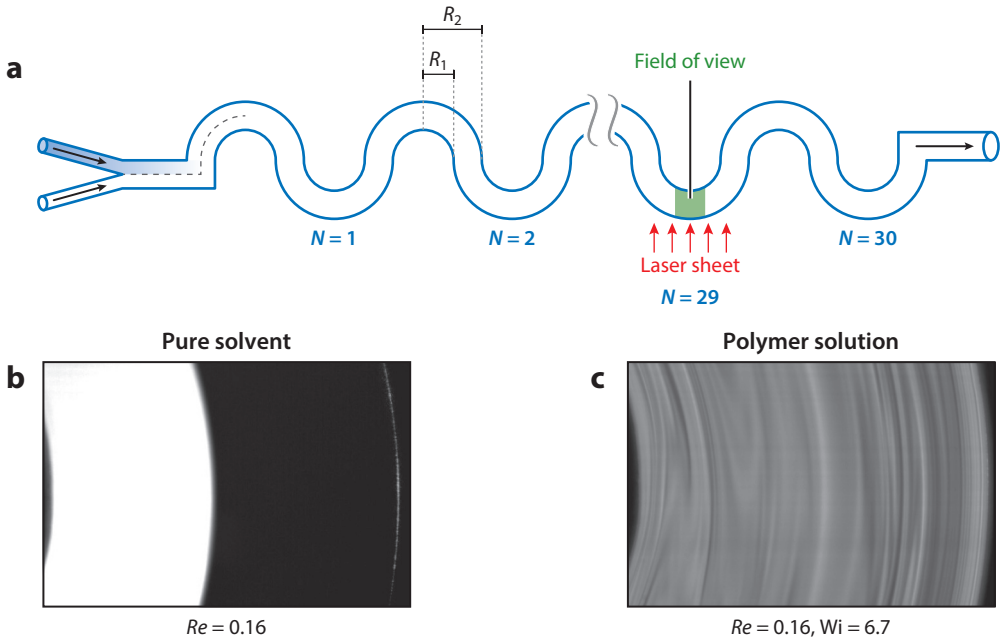

Figure 8

(*a*) Schematic of a curvilinear channel. (*b*,*c*) Snapshots of flow mixing taken with a laser visualization sheet at location $N = 29$ in the channel, for (*b*) a pure solvent at $Re = 0.16$ and (*c*) a polymer solution at the same flow rate corresponding to $Wi = 6.7$. Bright regions correspond to high concentrations of the fluorescent dye. Figure adapted with ppermission from Groisman & Steinberg (2001b).

5.1. Mixing Enhancement and the Lagrangian Approach to Pair Dispersion in Elastic Turbulence

As Groisman & Steinberg (2001b) showed quantitatively for the first time, ET causes an efficient mixing visualized by fluorescent dye (passive tracer) with a characteristic mixing time up to four orders of magnitude smaller than that of their molecular diffusion (see **Figure 8**). A more elaborate quantitative approach has revealed a key role of the velocity boundary layer near the wall in reducing mixing efficiency (Chertkov & Lebedev 2003; Burghelea et al. 2004a,b; Chernykh & Lebedev 2008; Jun & Steinberg 2010). Due to a reduced velocity near the wall, the boundary layer becomes a sink for passive tracers. The numerical simulations and experiment disclose that vigorous, random, and localized excursions of the tracers trapped near the walls strongly perturb the passive scalar distribution in the peripheral and bulk regions and cause growth of the mixing length (Chernykh & Lebedev 2008, Jun & Steinberg 2010). An intermittent ejection of the tracers into the bulk, surprisingly analogous to the intermittent injection of the elastic stresses in ET, reduces the effectiveness of mixing, increases the mixing length, and causes a stronger power law dependence of the mixing length on the Peclet number, $\sim Pe^{1/4}$, than the $\sim \ln Pe$ dependence in an unbounded vessel, where $Pe = V_{\rm rms} l/D$ is the ratio of the velocity to diffusion mass transfer (Batchelor 1959). The dependence of the new length scale, the mixing boundary layer W, on the small parameter $Pe^{-1} \ll 1$ is predicted to scale as $W \sim Pe^{-1/4} \sim D^{1/4}$ (Chertkov & Lebedev 2003), and has been confirmed by experiment (Burghelea et al. 2004b). It is quite remarkable that it is analogous to scaling of the velocity boundary layer width, $w \sim \eta^{1/4}$, discussed above (**Figure 5** and Burghelea et al. 2007). Finally, the Batchelor prediction of k^{-1} decay of the passive scalar power spectrum was verified by Jun & Steinberg (2010).

To achieve a fundamental understanding of mixing and transport phenomena, one needs to relate them to an underlying microscopic-level description, such as a particle pairs dispersion, which has been expected to show an exponential particle pair separation on average and an asymptotically exponential particle pair separation in time in smooth, temporally random flow. However, an experiment in ET has revealed that the pair dispersion is ballistic and shows no signature of the asymptotic exponential growth for sufficiently long times (Afik & Steinberg 2017). Later numerical simulations have indeed confirmed that the particle separation initially grows ballistically, and that exponential growth is only observed after extremely long times above $200\tau_\zeta$, where τ_ζ is the Kolmogorov timescale (Dharivat & Bragg 2018).

5.2. Experimental Tests of the Elastic Turbulence Theory Assumptions: Macroscopic and Microscopic Approaches

As discussed in Section 3.3, the two main assumptions and the Oldroyd-B linear model on which the theory is based (Balkovsky et al. 2001, Fouxon & Lebedev 2003) have been tested experimentally and numerically on both macroscopic and microscopic scales. The tests have revealed significant discrepancies between the experimental results and the theory (Balkovsky et al. 2001, Fouxon & Lebedev 2003), which are summarized below. (*a*) Elastic stress exceeds viscous stress by up to two orders of magnitude in ET, as shown in an experiment with molecular sensors (see figure 4 of Liu & Steinberg 2010a) and in numerical simulations (Berti et al. 2008). (*b*) The rms velocity gradients or $Wi_{\rm loc}$ are not saturated but grow with Wi in ET and exceed the predicted value of $Wi_{\rm loc} \approx 1$ by up to two orders of magnitude, as shown in **Figure 5** (bottom left inset) and **Figure 7*c*,*d***. The latter is a consequence of the Oldroyd-B model used in the theory and of the assumption $R_{\rm back} \ll R_{\rm max}$, both of which disagree with experiment (Gerashchenko et al. 2005; Liu & Steinberg 2010a,b, 2014). One way out of this discrepancy is to use, e.g., the FENE model to overcome the infinite polymer extensibility (Chertkov 2000, Thiffeault 2003, Afonso & Vincenzi 2005, Davoudi & Schumacher 2006, Bagheri et al. 2012). (*c*) The maximum value of the elastic stress $\sigma_{\rm p}^{\rm s}$ exceeds the predicted value of $\sigma_{\rm p} \approx 0.01$ Pa by more than two orders of magnitude; hence for the molecular sensor T4 DNA, one gets $\sigma_{\rm p}^{\rm s} \approx 5$ Pa (see figure 5 of Liu & Steinberg 2010a). However, the most remarkable results of these studies are the linear relation $\sigma_{\rm p}/(\eta/\lambda) \approx 130 Wi_{\rm loc}$, found for T4 DNA in the entire ET regime in a wide range of ϕ, and its saturation at the highest value of $Wi_{\rm loc} \simeq 30$ for all ϕ at $\sigma_{\rm p}^{\rm s}\lambda/\eta \approx 3{,}000$, corresponding to ∼5 Pa (see figure 7 of Liu & Steinberg 2010a). The value of the coefficient in the linear relation is probably related to the nonlinear elastic properties of T4 DNA and may vary for other polymers. Thus, one concludes that $Wi_{\rm loc}$ is the only relevant control parameter in ET that uniquely determines the elastic stress in the ET flow.

6. NEW DIRECTION: ELASTIC TURBULENCE IN A FLOW WITHOUT LATERAL WALLS

To resolve the evident discrepancy between the only existing theory of ET in unbounded, homogeneous, and isotropic flow (Fouxon & Lebedev 2003) and the bounded, inhomogeneous, and anisotropic flow studied experimentally (Groisman & Steinberg 2000, 2001b), Varshney & Steinberg (2017) have suggested to study a viscoelastic fluid flow between two widely spaced obstacles hindering a channel flow, where the channel walls are located sufficiently far from the obstacles (see **Figure 9*a***), as a paradigm of an experimentally realizable unbounded and homogeneous flow of a viscous polymer solution at $Re \ll 1$ and $Wi \gg 1$. As the result of elastic instabilities, a pair of counter-rotating elongated vortices that fill a space between two obstacles in its length and width present two mixing layers with nonuniform cross-stream shear velocity profiles.

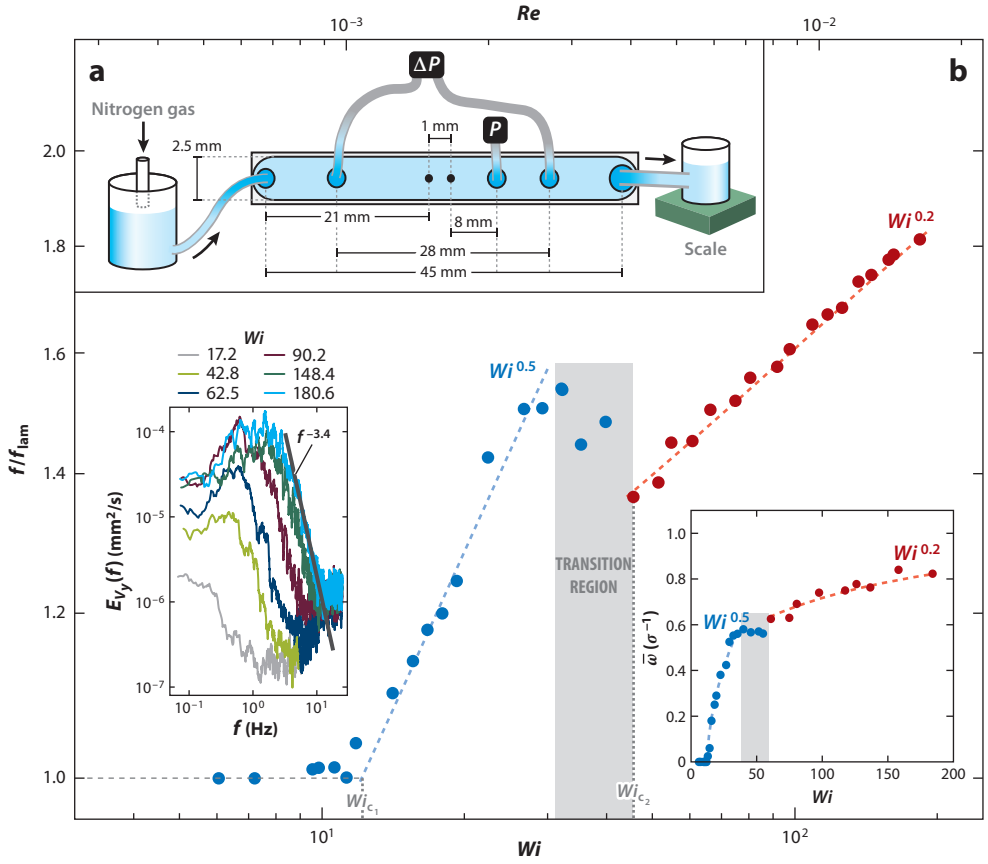

Figure 9

(*a*) Experimental setup of a channel with two obstacles hindering a channel flow (not to scale). A differential pressure sensor, labeled ΔP, is used to measure the pressure drop across the obstacles. An absolute pressure sensor, labeled P, after the downstream cylinder is used to obtain measurements of pressure fluctuations. (*b*) Normalized friction factor f/f_{lam} plotted against Wi, where the dashed lines are the fits above the first instability, $f/f_{\text{lam}} \sim Wi^{0.5}$, and in the ET regime, $f/f_{\text{lam}} \sim Wi^{0.2}$, which yield the critical values for the respective transitions, $Wi_{c_1} \approx 12$ and $Wi_{c_2} \approx 45$. (*Left inset*) The frequency power spectra of the cross-stream velocity $E_{V_y}(f)$ in log-log presentation for six values of Wi. The dashed line indicates the power spectrum decay with the exponent $\alpha \approx -3.4 \pm 0.1$ in the elastic turbulence regime. (*Right inset*) Spatially (region between the obstacles) and temporally (≈100 s) averaged vorticity $\bar{\omega}$ plotted against Wi, where the dashed lines are the fits, $\bar{\omega} \sim Wi^{0.5}$ and $\bar{\omega} \sim Wi^{0.2}$. The gray band indicates the transition region. Figure adapted with permission from Varshney & Steinberg (2018a).

6.1. Vorticity Enhancement and a Possible Kelvin–Helmholtz Instability

The flow between two obstacles is characterized by the dependence of the normalized friction factor f/f_{lam} on Wi, which reveals two scaling regimes: At $Wi_{c_1} \approx 12$ and up to $Wi \approx 30$, f/f_{lam} grows as $Wi^{0.5}$, and at $Wi > Wi_{c_2} \approx 45$, f/f_{lam} grows as $Wi^{0.2}$; these regions are separated by a transition region at $30 \leq Wi \leq 45$ characterized by a slight reduction of f/f_{lam}. Here, Wi_{c_1} and Wi_{c_2} are the elastic instability and ET onsets, respectively (**Figure 9*b***). It is remarkable that the same scaling relations are observed in the same two Wi regions for the spatially and temporally (over ∼100 s) averaged vorticity $\bar{\omega}$ growth (**Figure 9*b***, right inset), in contrast to the well-known result that polymer additives inhibit vorticity but at larger Re (Cadot & Lebey 1999, Cressman et al. 2001). The ET regime at $Wi > Wi_{c_2}$ is described by a characteristic power law decay of the

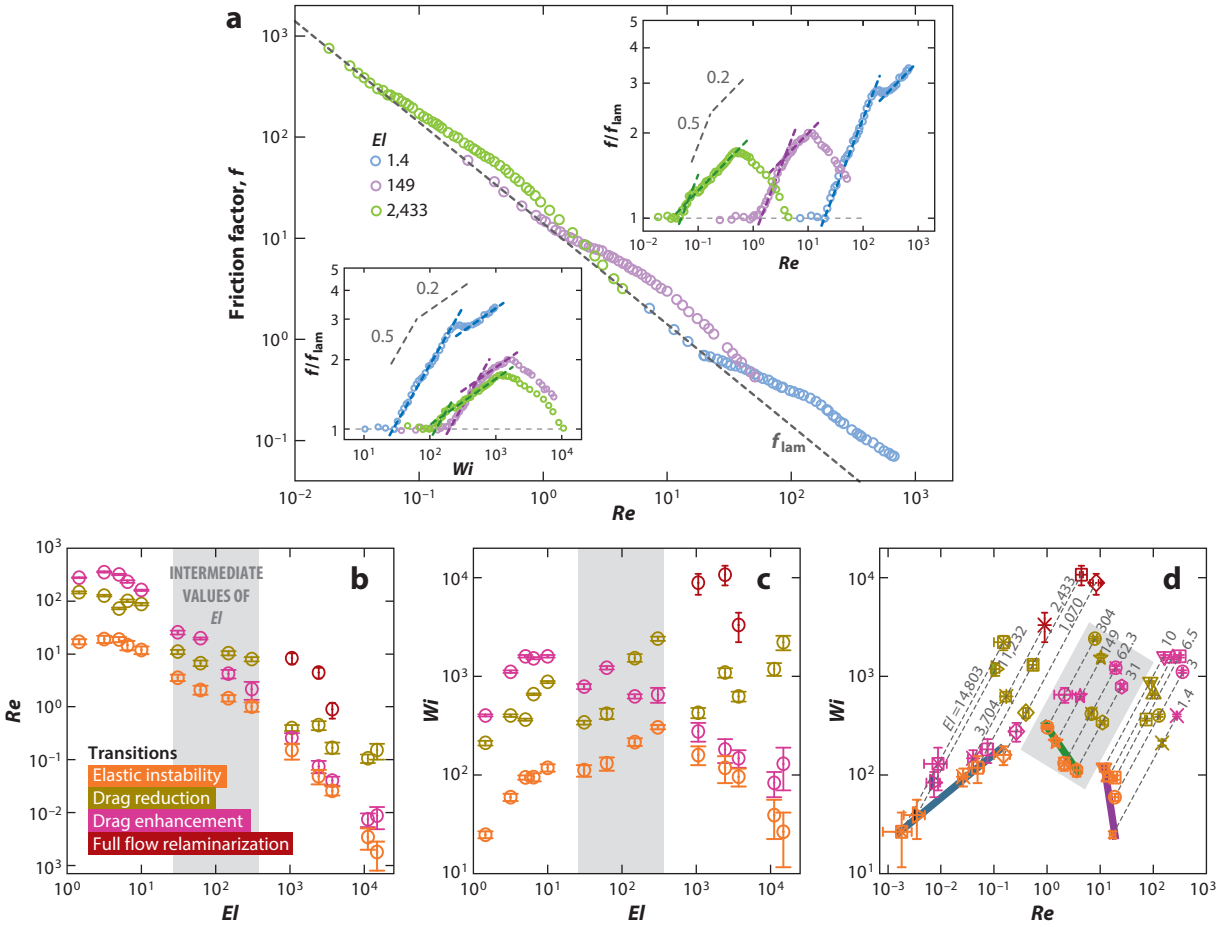

Figure 10

(*a*) Friction factor f plotted against Re for three values of El. The dashed line $f_{lam} \sim 1/Re$ represents the laminar flow. (*Top inset*) Normalized friction factor f/f_{lam} plotted against Re. (*Bottom inset*) The same data presented as f/f_{lam} plotted against Wi, with the fits marked by dashed lines in two regions: $f/f_{lam} \sim Wi^{0.5}$ above the elastic instability and $f/f_{lam} \sim Wi^{0.2}$ in the elastic turbulence regime. The drag reduction for $El = 2{,}433$ occurs at $Re \approx 0.5$ and $Wi \approx 1{,}216$ and continues until the flow fully relaminarizes. (*b–d*) Stability diagram of different flow regimes in (*b*) (Re, El), (*c*) (Wi, El) and (*d*) (Wi, Re) coordinates. The gray band in panels *b–d* indicates the region of intermediate values of El. Solid lines of different colors in subpanel *d* are used as a guide to track the transition in different regions. Figure adapted with permission from Varshney & Steinberg (2018b).

cross-stream velocity power spectrum with $\alpha \approx 3.4$, typical for ET (**Figure 9*b***, left inset). In the ET regime, $\nabla \cdot \mathbf{V}(x, y)$ in a 2D plane is found to be close to zero, indicating that the velocity field is 2D and homogeneous (see supplemental figure 4SM of Varshney & Steinberg 2018a). However, the main message of the velocity field analysis via PIV measurements is the generation of small vortices inside two mixing layers above the ET onset, which is quantitatively characterized by the growth of the circulation of small vortices with the same scaling exponent as $\bar{\omega}$ (figure 5 of Varshney & Steinberg 2018a). This observation is reminiscent of the Kelvin–Helmholtz instability of a mixing layer in a Newtonian fluid at $Re \gg 1$, which plays a key role in instabilities of parallel shear flows in their transition to turbulence. Further studies of a possible elastic analog of Kelvin-Helmholtz instability in viscoelastic creeping flows may shed light on the transition to ET in

such parallel shear flows, an important subject not discussed in this review since it is just at the beginning of its development (Morozov & van Saarloos 2007, Pan et al. 2013).

6.2. Inertial Effect in Elastic Turbulence

Using the same setup of a flow between two widely spaced obstacles hindering a channel flow (**Figure 9*a***), one can extend the range of *Re* and *Wi* to much higher values to explore the effect of inertia on the stability of a viscoelastic flow in a broad range of the control parameters *El*, *Re*, and *Wi* (Varshney & Steinberg 2018b). Varying solvent viscosity η_s by two orders of magnitude allows one to tune $El = \lambda(\eta_s)\eta_s/\rho D^2 \sim \eta_s^2/\rho D^2$ by more than four orders of magnitude (Varshney & Steinberg 2018b). Such an approach enables researchers to investigate the role of inertia in viscoelastic flows in different flow regimes in a wide range of (*Re*, *Wi*) and *El*. It is well known that in inertia-dominated flow at high *Re* and low *El*, a reduction in turbulent friction drag occurs due to intricate competition between inertial and elastic stresses, as shown recently in EIT at $Re \gg 1$ and $Wi \gg 1$ (Samanta et al. 2013). This exhibits properties similar to ET despite the fact that it is driven by both inertial and elastic stresses, and their interplay defines EIT properties (Dubief et al. 2013, Samanta et al. 2013). Thus, a fundamental question arises: How does the inertial effect modify ET in a viscoelastic flow by increasing *Re* toward EIT and TDR?

Using the normalized friction coefficient f/f_{lam} and the pressure power spectrum $E_{pp}(f)$ obtained in a wide range of the control parameters, researchers have revealed (*a*) the presence of three flow regimes with distinctive scaling behaviors in both f/f_{lam} (**Figure 10*a***) and $E_{pp}(f)$ and (*b*) three regions on the stability diagrams in the parameter space of *Re*, *Wi*, and *El* depending on the value of *El* (**Figure 10*b–d***). In spite of the fact that rather high values of *Re* are reached, inertial turbulence is not attained in the region between the obstacles and in channel flow outside this region (Varshney & Steinberg 2018b). In the drag enhancement regime in ET at high *El*, one observes the scaling $f/f_{lam} \sim Wi^{0.2}$ for the friction coefficient and the exponents $\beta \sim 3$ and $\alpha \sim 3.4$ for the pressure and velocity spectrum decays, respectively (Varshney & Steinberg 2018a). Remarkably, for $El = 1.4$, $Re \gtrsim 845$, and $Wi \lesssim 1{,}220$ (see **Figure 10*a*** and Varshney & Steinberg 2018b), the scaling exponents are found to be rather close, $f/f_{lam} \sim Wi^{0.2}$ and $\beta \cong 3$. However, the most striking result is the discovery of a complete relaminarization of viscoelastic flows at $El \gg 1$ and $Re \leq 1$, different from the well-known TDR (**Figure 10*a***). Further studies at higher *Re* and a quantitative characterization of the velocity field via PIV and laser Doppler velocimetry may uncover the role of inertial effects in ET and its relation to EIT.

SUMMARY POINTS

1. The key features of elastic turbulence (ET) are independent of flow geometry.
2. Probability density functions and the power spectrum decay exponent of the pressure fluctuations are the same for a wide range of Weissenberg number (*Wi*) and polymer concentrations.
3. ET theory correctly explains the power law decay exponent of the velocity power spectrum, but its assumptions contradict experiments.
4. Boundary layer width is a new length scale, $w \ll L$, in wall-bounded ET.
5. Elastic waves in ET have been observed, and their speed provides value of averaged elastic stress.

6. Unexpected vortex amplification and complete relaminarization in ET at Reynolds number $Re \leq 1$ have ben discovered in viscoelastic flows between two obstacles hindering channel flow.

FUTURE ISSUES

1. To completely characterize ET, as well as elasto-inertial turbulence and turbulent drag reduction, we need a new approach to measure the elastic stress's spectral and statistical properties, as well as its dynamics.
2. A new theory of ET is required based on a nonlinear polymer model to verify scaling relations between velocity, pressure, and elastic stress.
3. Interaction between coherent structures and fluctuations that provides information about energy transfer between polymer and velocity fields in ET is needed.

DISCLOSURE STATEMENT

The author is not aware of any biases that might be perceived as affecting the objectivity of this review.

ACKNOWLEDGMENTS

I am in particular grateful to V. Lebedev and M. Chertkov for numerous and fruitful discussions; to G. Falkovich, K. Turitsyn, S. Vergeles, and I. Fouxon for theoretical discussions over the years; and to my longtime collaborators A. Groisman, E. Segre, T. Burghelea, C. Chevallard, S. Gerashchenko, Y. Jun, Y. Liu, E. Afik, and A. Varshney. I am particularly indebted to A. Groisman, with whom I have shared the joy of discovery. This work was partially supported by Israel Science Foundation (ISF) grant 882/15 and by United States–Israel Binational Science Foundation (BSF) grant 2016145.

LITERATURE CITED

Abed WM, Whalley RD, Dennis DJC, Poole RJ. 2016. Experimental investigation of the impact of elastic turbulence on heat transfer in a serpentine channel. *J. Non-Newton. Fluid Mech.* 231:68–78

Afik E, Steinberg V. 2017. On the role of initial velocities in pair dispersion in a microfluidic chaotic flow. *Nat. Commun.* 8:468

Afonso MM, Vincenzi D. 2005. Nonlinear elastic polymers in random flow. *J. Fluid Mech.* 540:99–109

Al-Mubaiyedh UA, Sureshkumar R, Khomami B. 1999. Influence of energetics on the stability of viscoelastic Taylor–Couette flow. *Phys. Fluids* 11:3217–26

Al-Mubaiyedh UA, Sureshkumar R, Khomami B. 2000. Linear stability of viscoelastic Taylor–Couette flow: influence of fluid rheology and energetics. *J. Rheol.* 44:1121–38

Al-Mubaiyedh UA, Sureshkumar R, Khomami B. 2002. Nonlinear stability of viscoelastic Taylor–Couette flow in the presence of viscous heating. *Phys. Fluids* 14:1056–64

Arratia PE, Thomas CC, Diorio J, Gollub JP. 2006. Elastic instabilities of polymer solutions in cross-channel flow. *Phys. Rev. Lett.* 96:144502

Avgousti M, Beris AN. 1993. Viscoelastic Taylor–Couette flow: bifurcation analysis in the presence of symmetries. *Proc. R. Soc. Lond. A* 443:17–37

Bagheri F, Mitra D, Perlekar P, Brandt L. 2012. Statistics of polymer extension in turbulent channel flow. *Phys. Rev. E* 86:056314

Balkovsky E, Fouxon A, Lebedev V. 2000. Turbulent dynamics of polymer solutions. *Phys. Rev. Lett.* 84:4765–68

Balkovsky E, Fouxon A, Lebedev V. 2001. Turbulence of polymer solutions. *Phys. Rev. E* 64:056301

Batchelor GK. 1959. Small-scale variation of convected quantities like temperature in turbulent flow. *J. Fluid Mech.* 5:113–33

Baumert BM, Muller SJ. 1995. Flow visualization of the elastic Taylor–Couette instability in Boger fluids. *Rheol. Acta* 34:147–59

Baumert BM, Muller SJ. 1997. Flow regimes in model viscoelastic fluids in a circular Couette system with independently rotating cylinders. *Phys. Fluids* 9:566–86

Baumert BM, Muller SJ. 1999. Axisymmetric and non-axisymmetric elastic and inertio-elastic instabilities in Taylor–Couette flow. *J. Non-Newton. Fluid Mech.* 83:33–69

Belan S, Chernykh A, Lebedev V. 2018. Boundary layer of elastic turbulence. *J. Fluid Mech.* 855:910–21

Berti S, Bistagnino A, Boffetta G, Celani A, Musacchio S. 2008. Two-dimensional elastic turbulence. *Phys. Rev. E* 77:055306(R)

Berti S, Boffetta G. 2010. Elastic waves and transition to elastic turbulence in a two-dimensional viscoelastic Kolmogorov flow. *Phys. Rev. E* 82:036314

Bird RB, Curtiss CF, Armstrong RC, Hassager O. 1987. *Dynamics of Polymeric Liquids*. New York: Wiley

Boffetta G, Celani A, Musacchio S. 2003. Two-dimensional turbulence of dilute polymer solutions. *Phys. Rev. Lett.* 91:034501

Brand H, Hohenberg PC, Steinberg V. 1984. Codimension-2 bifurcations for convection in binary fluid mixtures. *Phys. Rev. A* 30:2548–61

Burghelea T, Segre E, Bar-Joseph I, Groisman A, Steinberg V. 2004a. Chaotic flow and efficient mixing in a microchannel with a polymer solution. *Phys. Rev. E* 69:066305

Burghelea T, Segre E, Steinberg V. 2004b. Mixing by polymers: experimental test of decay regime of mixing. *Phys. Rev. Lett.* 92:164501

Burghelea T, Segre E, Steinberg V. 2005. Validity of the Taylor hypothesis in a random spatially smooth flow. *Phys. Fluids* 17:103101

Burghelea T, Segre E, Steinberg V. 2006. Role of elastic stress in statistical and scaling properties of elastic turbulence. *Phys. Rev. Lett.* 96:214502

Burghelea T, Segre E, Steinberg V. 2007. Elastic turbulence in von Karman swirling flow between two disks. *Phys. Fluids* 19:053104

Byars JA, Oeztekin A, Brown RA, McKinley GH. 1994. Spiral instabilities in the flow of highly elastic fluids between rotating parallel disks. *J. Fluid. Mech.* 271:173–218

Cadot O, Lebey M. 1999. Shear instability inhibition in a cylinder wake by local injection of a viscoelastic fluid. *Phys. Fluids* 11:494–96

Celani A, Musacchio S, Vincenzi D. 2005. Polymer transport in random flow. *J. Statist. Phys.* 118:531–54

Chernykh A, Lebedev V. 2008. Passive scalar structures in peripheral regions of random flows. *JETP Lett.* 87:682–86

Chertkov M. 2000. Polymer stretching by turbulence. *Phys. Rev. Lett.* 84:4761–64

Chertkov M, Kolokolov I, Lebedev V, Turitsyn K. 2005. Polymer statistics in a random flow with mean shear. *J. Fluid Mech.* 531:251–60

Chertkov M, Lebedev V. 2003. Decay of scalar turbulence revisited. *Phys. Rev. Lett.* 90:034501

Clarke A, Howe AM, Mitchell J, Staniland J, Hawkes L, Leepera K. 2015. Mechanism of anomalously increased oil displacement with aqueous viscoelastic polymer solutions. *Soft Matter* 11:3536–41

Cressman JR, Baley Q, Goldburg WI. 2001. Modification of a vortex street by a polymer additive. *Phys. Fluids* 13:867

Cross MC, Hohenberg PC. 1993. Pattern formation outside of equilibrium. *Rev. Mod. Phys.* 65:851–1112

Crumeyrolle O, Mutabazi I, Grisel M. 2002. Experimental study of inertioelastic Couette–Taylor instability modes in dilute and semidilute solutions. *Phys. Fluids* 14:1681–88

Davoudi J, Schumacher J. 2006. Stretching of polymers around the Kolmogorov scale in a turbulent shear flow. *Phys. Fluids* 18:025103

De Angelis E, Casciola CM, Piva R. 2012. Energy spectra in viscoelastic turbulence. *Physica D* 241:297–303

de Gennes PG. 1986. Towards a scaling theory of drag reduction. *Physica A* 140:9–25

Denn MM. 1990. Issues in viscoelastic fluid mechanics. *Ann. Rev. Fluid Mech.*22:13–32

Dharivat R, Bragg AD. 2018. Fluid particles only separate exponentially in the dissipation range of turbulence after extremely long times. *Phys. Rev. Fluids* 3:034604

Drazin PG, Reid WH. 1982. *Hydrodynamic Stability*. Cambridge, UK: Cambridge Univ. Press

Dubief Y, Terrapon VE, Soria J. 2013. On the mechanism of elasto-inertial turbulence. *Phys. Fluids* 25:110817

Eckhardt B, Kronjäger J, Schumacher J. 2002. Stretching of polymers in a turbulent environment. *Comput. Phys. Commun.* 147:538–43

Fouxon A, Lebedev V. 2003. Spectra of turbulence in dilute polymer solutions. *Phys. Fluids* 15:2060–72

Gan HY, Lam YC, Nguyen N-T. 2006. Polymer-based device for efficient mixing of viscoelastic fluids. *Appl. Phys. Lett.* 88:224103

Gerashchenko S, Chevallard C, Steinberg V. 2005. Single polymer dynamics: coil-stretch transition in a random flow. *Europhys. Lett.* 71:221–27

Giesekus H. 1968. Nicht-lineare Effekte beim Strömen viskoelastischer Flussigkeiten durch Schlitz- und Lochdüsen. *Rheol. Acta* 7:127–38

Giesekus H. 1972. On instabilities in Poiseuille and Couette flows of viscoelastic fluids. *Prog. Heat Mass Transf.* 5:187–93

Grilli M, Vázquez-Quesada A, Ellero M. 2013. Transition to turbulence and mixing in a viscoelastic fluid flowing inside a channel with a periodic array of cylindrical obstacles. *Phys. Rev. Lett.* 110:174501

Groisman A. 1993. *Experiments on the Couette–Taylor flow with dilute polymer solutions*. M.Sc. Thesis, Weizmann Inst. Sci., Rehovot, Israel

Groisman A, Steinberg V. 1996. Couette–Taylor flow in dilute polymer solutions. *Phys. Rev. Lett.* 77:1480–83

Groisman A, Steinberg V. 1997. Solitary vortex pairs in viscoelastic Couette flow. *Phys. Rev. Lett.* 78:1460–63

Groisman A, Steinberg V. 1998a. Elastic versus inertial instability in a polymer solution flow. *Europhys. Lett.* 43:165–70

Groisman A, Steinberg V. 1998b. Mechanism of elastic instability in Couette flow of polymer solutions: experiment. *Phys. Fluids* 10:2451–63

Groisman A, Steinberg V. 2000. Elastic turbulence in a polymer solution flow. *Nature* 405:53–55

Groisman A, Steinberg V. 2001a. Efficient mixing at low Reynolds numbers using polymer additives. *Nature* 410:905–8

Groisman A, Steinberg V. 2001b. Stretching of polymers in a random three-dimensional flow. *Phys. Rev. Lett.* 86:934–37

Groisman A, Steinberg V. 2004. Elastic turbulence in curvilinear flows of polymer solutions. *New J. Phys.* 6:29–48

Gupta A, Pandit R. 2017. Melting of a nonequilibrium vortex crystal in a fluid film with polymers: elastic versus fluid turbulence. *Phys. Rev. E* 95:033119

Haward SJ, McKinley GH. 2013. Instabilities in stagnation point flows of polymer solutions. *Phys. Fluids* 25:083104

Hinch EJ. 1977. Mechanical models of dilute polymer solutions in strong flows. *Phys. Fluids* 20:S22–30

Howe AM, Clarke A, Giernalczyk D. 2015. Flow of concentrated viscoelastic polymer solutions in porous media: effect of M(W) and concentration on elastic turbulence onset in various geometries. *Soft Matter* 11:6419–31

Hur J, Shaqfeh E, Babcock H, Chu S. 2002. Dynamics and configurational fluctuations of single DNA molecules in linear mixed flows. *Phys. Rev. E* 66:011915

Joo YL, Shaqfeh ESG. 1992. A purely elastic instability in Dean and Taylor–Dean flow. *Phys. Fluids A* 4:524–42

Joo YL, Shaqfeh ESG. 1994. Observations of purely elastic instabilities in the Taylor–Dean flow of a Boger fluid. *J. Fluid Mech.* 262:27–73

Joseph DD. 1990. *Fluid Dynamics of Viscoelastic Liquids*. New York: Springer-Verlag

Joseph DD, Narain A, Riccius O. 1986a. Shear-wave speeds and elastic moduli for different liquids. Part 1. Theory. *J. Fluid Mech.* 171:309–38

Joseph DD, Riccius O, Arney M. 1986b. Shear-wave speeds and elastic moduli for different liquids. Part 2. Experiments. *J. Fluid Mech.* 171:289–308

Jun Y, Steinberg V. 2009. Power and pressure fluctuations in elastic turbulence over a wide range of polymer concentrations. *Phys. Rev. Lett.* 102:124503

Jun Y, Steinberg V. 2010. Mixing of passive tracers in the decay Batchelor regime of a channel flow. *Phys. Fluids* 22:123101

Jun Y, Steinberg V. 2011. Elastic turbulence in a curvilinear channel flow. *Phys. Rev. E* 84:056325

Jun Y, Steinberg V. 2017. Polymer concentration and properties of elastic turbulence in a von Karman swirling flow. *Phys. Rev. Fluids* 2:103301

Kenney S, Poper K, Chapagain G, Christopher GF. 2013. Large Deborah number flows around confined microfluidic cylinders. *Rheol. Acta* 52:485–97

Khomami B, Moren LD. 1997. Stability of viscoelastic flow around periodic array of cylinders. *Rheol. Acta* 36:367–83

Kumar KA, Graham MD. 2000. Solitary coherent structures in viscoelastic shear flow: computation and mechanism. *Phys. Rev. Lett.* 85:4056–59

Landau LD, Lifschitz EM. 1987. *Fluid Mechanics*. Oxford, UK: Pergamon

Landau LD, Lifschitz EM. 1989. *Electrodynamics of Continuous Media*. Oxford, UK: Pergamon

Larson RG. 1992. Instabilities in viscoelastic flows. *Rheol. Acta* 31:213–63

Larson RG, Muller SJ, Shaqfeh ESG. 1994. The effect of fluid rheology on the elastic Taylor–Couette instability. *J. Non-Newton. Fluid Mech.* 51:195–225

Larson RG, Shaqfeh ESG, Muller SJ. 1990. A purely elastic instability in Taylor–Couette flow. *J. Fluid Mech.* 218:573–600

Latrache N, Abcha N, Crumeyrolle O, Mutabazi I. 2016. Defect-mediated turbulence in ribbons of viscoelastic Taylor–Couette flow. *Phys. Rev. E* 93:043126

Li D-Y, Li X-B, Zhang H-N, Li F-C, Qian S, Joo SW. 2017. Efficient heat transfer enhancement by elastic turbulence with polymer solution in a curved microchannel. *Microfluid. Nanofluid.* 21:10

Li F-C, Zhang H-N, Cao Y, Kunugi T, Kinoshita H, Oshima M. 2012. A purely elastic instability and mixing enhancement in a 3D curvilinear channel flow. *Chin. Phys. Lett.* 29:094704

Li X-B, Li F-C, Cai W-H, Zhang H-N, Yang J-C. 2012. Very-low-*Re* chaotic motions of viscoelastic fluid and its unique applications in microfluidic devices: a review. *Exp. Therm. Fluid Sci.* 39:1–16

Li X-B, Zhang HN, Cao Y, Oshima M, Li FC. 2015. Motion of passive scalar by elasticity-induced instability in curved microchannel. *Adv. Mech. Eng.* 6:734175

Liu N, Khomami B. 2013. Elastically induced turbulence in Taylor–Couette flow: direct numerical simulation and mechanistic insight. *J. Fluid Mech.* 737:R4

Liu Y, Steinberg V. 2010a. Molecular sensor of elastic stress in a random flow. *EPL* 90:44002

Liu Y, Steinberg V. 2010b. Stretching of polymer in a random flow: effect of a shear rate. *EPL* 90:44005

Liu Y, Steinberg V. 2014. Single polymer dynamics in a random flow. *Macromol. Symp.* 337:34–43

Lumley J. 1972. On the solution of equations describing small scale deformations. *Symp. Math.* 9:315–34

McKinley GH, Armstrong RC, Brown RA. 1993. The wake instability in viscoelastic flow past confined circular cylinders. *Philos. Trans. R. Soc. A* 344:265–304

McKinley GH, Byars JA, Brown RA, Armstrong RC. 1991. Observations on the elastic instability in cone-and-plate and parallel-plate flows of a polyisobutylene Boger fluid. *J. Non-Newton. Fluid Mech.* 40:201–29

Mitchell J, Lyons K, Howe AM, Clarke A. 2016. Viscoelastic polymer flows and elastic turbulence in three-dimensional porous structures. *Soft Matter* 12:460–68

Morozov AN, van Saarloos W. 2007. An introductory essay on subcritical instabilities and the transition to turbulence in visco-elastic parallel shear flows. *Phys. Rep.* 447:112–43

Muller SJ, Shaqfeh ESG, Larson RG. 1989. A purely elastic transition in Taylor–Couette flow. *Rheol. Acta* 28:499–503

Muller SJ, Shaqfeh ESG, Larson RG. 1993. Experimental studies of the onset of oscillatory instability in viscoelastic Taylor-Couette flow. *J. Non-Newton. Fluid Mech.* 46:315–30

Musacchio S, Vincenzi D. 2011. Deformation of a flexible polymer in a random flow with long correlation time. *J. Fluid Mech.* 670:326–36

Nguyen MQ, Delache A, Simoens S, Bos WJT, El Hajem M. 2016. Small scale dynamics of isotropic viscoelastic turbulence. *Phys. Rev. Fluids* 1:083301

Oeztekin A, Brown RA. 1993. Instability of a viscoelastic fluid between rotating parallel disks: analysis for the Oldroyd-B fluid. *J. Fluid Mech.* 255:473–502

Oeztekin A, Brown RA, McKinley GH. 1994. Quantitative prediction of the viscoelastic instability in cone-and plate flow of a Boger fluid using a multi-mode Giesekus model. *J. Non-Newton. Fluid Mech.* 54:351–77

Pan L, Morozov A, Wagner C, Arratia PE. 2013. Nonlinear elastic instability in channel flows at low Reynolds numbers. *Phys. Rev. Lett.* 110:174502

Perlekar P, Mitra D, Pandit R. 2010. Direct numerical simulations of statistically steady, homogeneous, isotropic fluid turbulence with polymer additives. *Phys. Rev. E* 82:066313

Poole RJ, Alves MA, Oliveira PJ. 2007. Purely elastic flow asymmetries. *Phys. Rev. Lett.* 99:164503

Poole RJ, Budhiraja B, Cain AR, Scott PA. 2012. Emulsification using elastic turbulence. *J. Non-Newton. Fluid Mech.* 177–78:15–18

Ray SS, Vincenzi D. 2016. Elastic turbulence in a shell model of polymer solution. *EPL* 114:44001

Samanta D, Dubief Y, Holzner M, Schaefer CH, Morozov A, et al. 2013. Elasto-inertial turbulence. *PNAS* 110:10557–62

Scholz CH, Wirner F, Gomez-Solano JR, Bechinger C. 2014. Enhanced dispersion by elastic turbulence in porous media. *EPL* 107:54003

Shaqfeh ESG. 1996. Purely elastic instabilities in viscometric flows. *Annu. Rev. Fluid Mech.* 28:129–85

Slutsky M, Steinberg V. 2005. Effective mixing and emulsification of very viscous substances by elastic turbulence. In *Report on the Horowitz Foundation Grant 3355*. Rehovot, Israel: Weizmann Inst. Sci.

Soulies A, Aubril J, Castelain C, Burghelea T. 2017. Characterization of elastic turbulence in a serpentine micro-channel. *Phys. Fluids* 29:083102

Steinberg V. 2019. Scaling relations in elastic turbulence. *Phys. Rev. Lett.* 123:234501

Steinberg V, Groisman A. 1998. Elastic versus inertial instability in Couette–Taylor flow of a polymer solution: review. *Philos. Mag. B* 78:253–63

Sureshkumar R, Beris AN, Avgousti M. 1994. Non-axisymmetric subcritical bifurcations in viscoelastic Taylor–Couette flow. *Proc. R. Soc. Lond. A* 447:135–53

Thiffeault J-L. 2003. Finite extension of polymers in turbulent flow. *Phys. Lett. A* 308:445–50

Thomas DG, Sureshkumar R, Khomami B. 2006. Pattern formation in Taylor–Couette flow of dilute polymer solutions: dynamical simulations and mechanism. *Phys. Rev. Lett.* 97:054501

Thomas DG, Sureshkumar R, Khomami B. 2009. Nonlinear dynamics of viscoelastic Taylor–Couette flow: effect of elasticity on pattern selection, molecular conformation and drag. *J. Fluid Mech.* 620:353–82

Toms BA. 1949. Some observation on the flow of linear polymer solutions through straight tubes at large Reynolds number. In *Proceedings of the 1st International Congress on Rheology*, Vol. 2, pp. 135–41. Amsterdam: North Holland

Traore B, Castelain C, Burghelea T. 2015. Efficient heat transfer in a regime of elastic turbulence. *J. Non-Newton. Fluid Mech.* 223:62–76

Tritton DJ. 1988. *Physical Fluid Dynamics*. Oxford, UK: Clarendon

Turitsyn K. 2007. Polymer dynamics in chaotic flows with strong shear component. *J. Exp. Theor. Phys.* 105:655–64

van Buel R, Schaaf C, Stark H. 2018. Elastic turbulence in two-dimensional Taylor–Couette flows. *EPL* 124:14001

Varshney A, Afik E, Kaplan Y, Steinberg V. 2016. Oscillatory elastic instabilities in an extensional viscoelastic flow. *Soft Matter* 12:2186–91

Varshney A, Steinberg V. 2017. Elastic wake instabilities in a creeping flow between two obstacles. *Phys. Rev. Fluids* 2:051301(R)

Varshney A, Steinberg V. 2018a. Drag enhancement and drag reduction in viscoelastic flow. *Phys. Rev. Fluids* 3:103302

Varshney A, Steinberg V. 2018b. Mixing layer instability and vorticity amplification in a creeping viscoelastic flow. *Phys. Rev. Fluids* 3:103303

Varshney A, Steinberg V. 2019. Elastic Alfven waves in elastic turbulence. *Nat. Commun.* 10:652

Vázquez-Quesada A, Ellero M. 2012. SPH simulations of a viscoelastic flow around a periodic array of cylinders confined in a channel. *J. Non-Newton. Fluid Mech.* 167–68:1–8

Vinogradov GV, Ivanova LI. 1967. Viscous properties of polymer melts and elastomers exemplified by ethylene-propylene copolymer. *Rheol. Acta* 6:209–22

Watanabe T, Gotoh T. 2010. Coil–stretch transition in an ensemble of polymers in isotropic turbulence. *Phys. Rev. E* 81:066301

Watanabe T, Gotoh T. 2013. Hybrid Eulerian–Lagrangian simulations for polymer–turbulence interactions. *J. Fluid Mech.* 717:535–71

Watanabe T, Gotoh T. 2014. Power-law spectra formed by stretching polymers in decaying isotropic turbulence. *Phys. Fluids* 26:035110

Whalley R, Abed WM, Dennis DJC, Poole RJ. 2015. Enhancing heat transfer at the micro-scale using elastic turbulence. *Theor. Appl. Mech. Lett.* 5:103–6

White JM, Muller SJ. 2000. Viscous heating and the stability of Newtonian and viscoelastic Taylor–Couette flows. *Phys. Rev. Lett.* 84:5130–33

White JM, Muller SJ. 2003. Experimental studies on the effect of viscous heating on the hydrodynamic stability of viscoelastic Taylor–Couette flow. *J. Rheol.* 47:1467–92